The Astrophysical Journal, 799:148 (27pp), 2015 February 1 doi:10.1088/0004-637X/799/2/148

ONE PLANE FOR ALL: MASSIVE STAR-FORMING AND QUIESCENT GALAXIES LIE ON THE SAME MASS FUNDAMENTAL PLANE AT $z \sim 0$ AND $z \sim 0.7$

Rachel Bezanson[1,4], Marijn Franx[2], and Pieter G. van Dokkum[3]
[1] Steward Observatory, Department of Astronomy, University of Arizona, Tucson, AZ 85721, USA
[2] Sterrewacht Leiden, Leiden University, NL-2300 RA Leiden, The Netherlands
[3] Department of Astronomy, Yale University, New Haven, CT 06520-8101, USA
Received 2014 August 29; accepted 2014 November 3; published 2015 January 23

ABSTRACT

Scaling relations between galaxy structures and dynamics have been studied extensively for early- and late-type galaxies, both in the local universe and at high redshifts. The abundant differences between the properties of disky and elliptical, or star-forming and quiescent, galaxies seem to be characteristic of the local universe; such clear distinctions begin to disintegrate as observations of massive galaxies probe higher redshifts. In this paper we investigate the existence of the mass fundamental plane of all massive galaxies ($\sigma \gtrsim 100\,\mathrm{km\,s^{-1}}$). This work includes local galaxies ($0.05 < z < 0.07$) from the Sloan Digital Sky Survey, in addition to 31 star-forming and 72 quiescent massive galaxies at intermediate redshift ($z \sim 0.7$) with absorption-line kinematics from deep Keck-DEIMOS spectra and structural parameters from *Hubble Space Telescope* imaging. In two-parameter scaling relations, star-forming and quiescent galaxies differ structurally and dynamically. However, we show that massive star-forming and quiescent galaxies lie on nearly the same mass fundamental plane, or the relationship between stellar mass surface density, stellar velocity dispersion, and effective radius. The scatter in this relation (measured about $\log\sigma$) is low: 0.072 dex (0.055 dex intrinsic) at $z \sim 0$ and 0.10 dex (0.08 dex intrinsic) at $z \sim 0.7$. This 3D surface is not unique: virial relations, with or without a dependence on luminosity profile shapes, can connect galaxy structures and stellar dynamics with similar scatter. This result builds on the recent finding that mass fundamental plane has been stable for early-type galaxies since $z \sim 2$. As we now find that this also holds for star-forming galaxies to $z \sim 0.7$, this implies that these scaling relations of galaxies will be minimally susceptible to progenitor biases owing to the evolving stellar populations, structures, and dynamics of galaxies through cosmic time.

Key words: cosmology: observations – galaxies: elliptical and lenticular, cD – galaxies: evolution – galaxies: fundamental parameters – galaxies: kinematics and dynamics – galaxies: spiral

Supporting material: machine-readable table

1. INTRODUCTION

Galaxy bimodality seems to be a fundamental property of the universe, especially at the present day. In the local universe, galaxies are either forming stars or not, and as a result of their differing stellar populations, their colors are generally blue or red (e.g., Blanton et al. 2003). In fact, the existence of massive quenched galaxies has been demonstrated as early as $z \sim 4$, only a couple billion years after the big bang (e.g., Straatman et al. 2014). Traditionally, scaling relations between global properties (sizes, luminosities or masses, and kinematics) of disk and elliptical galaxies have been studied separately to constrain their formation and evolutionary models. This approach is intuitive as late- and early-type galaxies differ in most ways in the local universe. Structurally, the stars in star-forming galaxies are generally flattened into disk-like formations, following exponential light profiles. Galaxies with quiescent stellar populations are rounder spheroids that follow de Vaucouleurs light profiles in projection. Furthermore, at fixed mass, quiescent galaxies are more compact than their star-forming counterparts (e.g., Shen et al. 2003). These populations also appear to differ dynamically: star-forming galaxies are primarily supported by rotation, and quiescent galaxies are dominated by dispersion support.

The relationship between rotational velocity and galaxy luminosity (or stellar mass), called the Tully–Fischer relation, describes the fundamental scaling of disk (star-forming) galaxies (e.g., Tully & Fisher 1977; Bell & de Jong 2001). Early-type (quiescent) galaxies lie on a similar scaling relation between the luminosity and velocity dispersion, called the Faber–Jackson relation (Faber & Jackson 1976). The scatter around this relation tightens when galaxy sizes are included, indicating that quiescent galaxies are better described by the three-parameter fundamental plane (e.g., Djorgovski & Davis 1987; Dressler et al. 1987). These relations have been used to constrain aspects of galaxy formation such as the growth of disks within dark matter halos (e.g., Fall & Efstathiou 1980; Blumenthal et al. 1986; Mo et al. 1998) and variations in the global mass-to-light ratios of elliptical galaxies (e.g., Faber 1987). Observationally, measurements of these scaling relations have been extended to high redshift, adding the dimension of time to further constrain formation of star-forming disks (e.g., Vogt et al. 1996; Weiner et al. 2006b; Kassin et al. 2007; Miller et al. 2012) or the aging of quiescent spheroids (e.g., van Dokkum & Franx 1996; van der Wel et al. 2004; van Dokkum & van der Marel 2007; Holden et al. 2010; Toft et al. 2012).

However, as observations of distant galaxies push to earlier epochs in the high-redshift universe, building evidence suggests that the clear distinctions between galaxy populations begin to break down. Populations of massive star-forming galaxies, which must be the progenitors of many of today's massive galaxies, increase in number density at higher redshift (e.g., Bell et al. 2004; Brammer et al. 2011; Whitaker et al. 2012; Muzzin et al. 2013; Tomczak et al. 2014). Dividing lines between

[4] Hubble Fellow.

structural properties and stellar populations become blurred as quiescent galaxies may appear more disk-like at higher redshifts ($z \gtrsim 1$; e.g., van der Wel et al. 2011; Weinzirl et al. 2011; Bruce et al. 2012; Chevance et al. 2012; Chang et al. 2013). As a result of the decreasing number density of quiescent galaxies with redshift, selection criteria based on either structural morphology or stellar populations designed to identify galaxies through cosmic time will be biased against a subset of the progenitors of those early galaxies. This "progenitor bias" (e.g., van Dokkum & Franx 1996) will become increasingly important as we connect the evolution of galaxies through earlier times.

As galaxy populations become less clearly bimodal at earlier epochs and individual galaxies likely transition between star-forming and quiescent periods, it would be preferable to define a flexible framework that allows for star-forming and quiescent galaxies to be studied together to allow for this ambiguity. In this paper, we examine the scaling relations between galaxy structures (light profile shapes and sizes), stellar masses (from stellar population synthesis modeling), and dynamics (velocity dispersions) for star-forming and quiescent galaxies alike. We examine these relations in the local universe ($0.05 < z < 0.07$) utilizing data from the Sloan Digital Sky Survey (SDSS) and at higher redshift ($z \sim 0.7$) using a deep spectroscopic survey collected with the DEIMOS spectrograph on Keck II in the COSMOS and UKIRT Infrared Deep Sky Survey (UKIDSS) Ultra Deep Survey (UDS) fields.

The paper is organized as follows: Section 2 provides an overview of the two data sets included in this analysis and describes the measured and derived properties of galaxies in those samples. Section 3 examines the 2D scaling relations between structural and dynamical properties of galaxies, highlighting the differences between star-forming and quiescent massive galaxies. Section 4 demonstrates the existence of a unified mass fundamental plane for both star-forming and quenched galaxies. In Section 5 we assess the ability of a variety of scaling relations to include both star-forming and quiescent galaxy populations, comparing measured scatter about each relation. Finally, in Section 6 we discuss the results of this work and highlight the implications for future studies of galaxy evolution. Throughout this paper we assume standard ΛCDM concordance cosmology with $H_0 = 70$ km s^{-1} Mpc^{-1}, $\Omega_M = 0.3$, and $\Omega_\Lambda = 0.7$. All magnitudes are quoted in the AB system.

2. DATA

2.1. SDSS Sample at $z \sim 0$

For our study of local galaxies, we use a sample of galaxies at $0.05 < z < 0.07$ from DR7 of the SDSS (Abazajian et al. 2009), selected as described in Bezanson et al. (2013). Galaxies are selected to have reliable spectroscopic measurements with *keep_flag* = 1, *z_warning* = 0, *sciencePrimary* = 1, and signal-to-noise ratio S/N > 20. Stellar mass-to-light ($M_\star/L$) ratios are acquired from the MPA-JHU galaxy catalog (Brinchmann et al. 2004). Best-fit Sérsic profiles in the r' band are included from Simard et al. (2011), and total stellar masses are calculated by scaling $M_\star/L$ to the total luminosity of the best-fit Sérsic profile (see Equation (7)). Effective radii are circularized, $r_e = R_{\rm hl}\sqrt{b/a}$, where $R_{\rm hl}$ is the semimajor half-light radius and b/a is the axis ratio. Velocity dispersions are taken from David Schlegel's *spZbest* catalog (*v_disp*) and are aperture corrected from the 3″ SDSS fiber to an effective radius using

$$\sigma_{\rm re} = \sigma_{\rm ap}(r_{\rm ap}/r_e)^{0.066} \quad (1)$$

from Cappellari et al. (2006). Only galaxies with <10% errors in velocity dispersion are included in the final sample.

Both star-forming and quiescent galaxies are included in this sample; the two populations are distinguished based on their colors. We calculate *K*-corrections to observed colors to $z = 0$ using KCORRECT (Blanton et al. 2003; Blanton & Roweis 2007). Finally, we adopt the $u-r$ and $r-z$ rest-frame color cuts from (Holden et al. 2012) to identify quiescent galaxies as

$$(u - r) > 2.26, \quad (2)$$

$$(r - z) < 0.75, \quad (3)$$

$$\text{and } (u - r) > 0.76 + 2.5(r - z). \quad (4)$$

These criteria have been demonstrated to separate star-forming and quiescent galaxies with only ∼18% contamination.

2.2. Keck-DEIMOS Sample at $z \sim 0.7$

Spectra for a total of 162 targeted galaxies were collected using the 1200 mm^{-1} grating, centered at 7800 Å. Spectra were reduced and extracted using the Spec2d pipeline (Cooper et al. 2012; Newman et al. 2013). Telluric corrections are applied by fitting models for atmospheric absorption, scaled to fit spectra in each mask. The resulting spectra have an average spectral range of ∼6500–9200 Å. The instrumental resolution, as measured from sky lines, was ∼1.6 Å at ∼7800 Å, which corresponds to $R \sim 5000$ or $\Delta v \sim 60$ km s^{-1}.

We observed a sample of galaxies at $0.4 < z < 0.9$ from the NEWFIRM Medium Band Survey (NMBS) COSMOS (Whitaker et al. 2011) and UKIDSS-UDS fields (Williams et al. 2009), focusing on overlap with the CANDELS (Grogin et al. 2011; Koekemoer et al. 2011)/3DHST (Brammer et al. 2012; Skelton et al. 2014) fields, using DEIMOS (Faber et al. 2003) on Keck II from 2012 January 19 to 21. Three masks were observed: two in NMBS-COSMOS with total exposures of 13.67 and 5.67 hr, and one in UDS for 7.67 hr. Weather and seeing conditions throughout the run were very good, with average seeing ranging from ∼0.″5 to 0.″7.

Galaxies were selected to span a range in *inferred velocity dispersion* (see, e.g., Bezanson et al. 2011) prioritizing galaxies with $\sigma_{\rm inf} \gtrsim 100$ km s^{-1}. We adopt the following definition of inferred velocity dispersion in this section and revisit possible definitions in Section 5:

$$\sigma_{\rm inf,V(n)} = \sqrt{\frac{GM_\star}{0.557 k_V R_e}}, \quad (5)$$

in which the virial constant depends on Sérsic index as

$$k_V(n) \approx 8.87 - 0.831n + 0.0241n^2 \quad (6)$$

(Cappellari et al. 2006). This includes the average ratio $\langle M_\star/M_{\rm dyn}\rangle \approx 0.557$ measured from a similar sample of galaxies in the SDSS in Bezanson et al. (2011).

This corresponds to a selection in size and mass ($\log M_\star > 10$), with no preselection on morphology. Therefore, the data set includes early- and late-type, or alternatively quiescent and star-forming, galaxies. Selection of these targets relative to the NMBS-COSMOS photometric catalog is presented in Figure 1. Additional properties of the sample (large symbols) are presented in Figure 3 relative to galaxies in the NMBS-COSMOS field within the same redshift range (gray dots). In addition

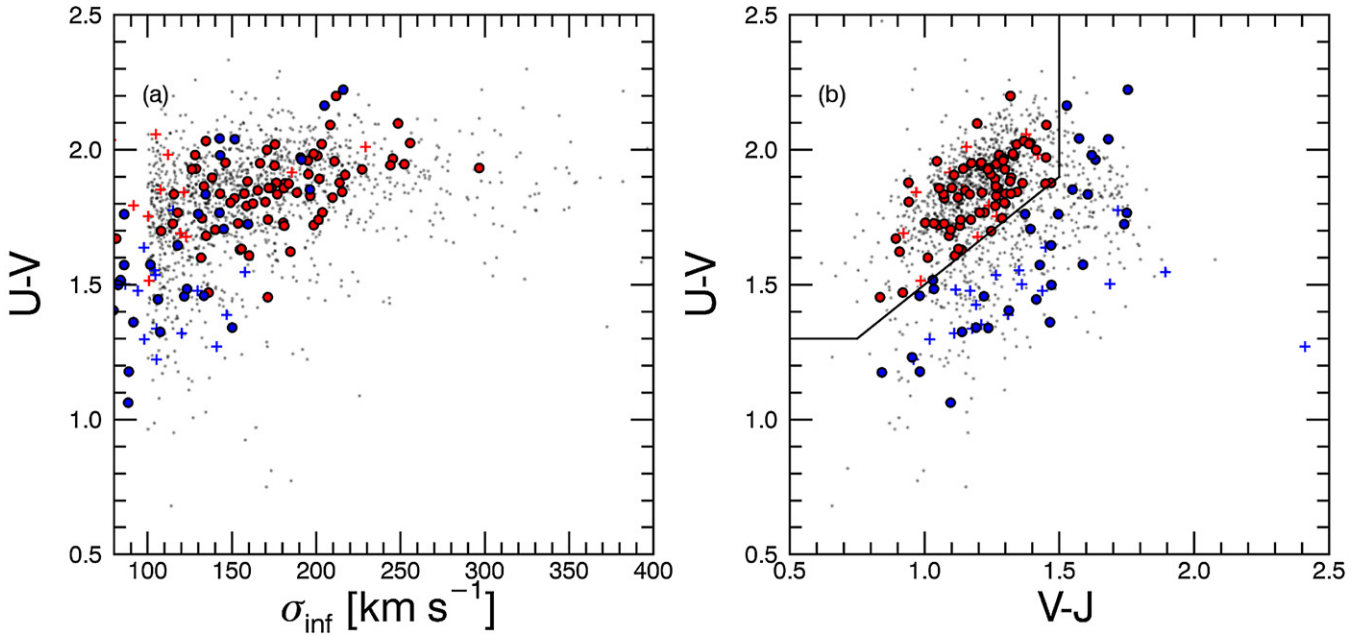

Figure 1. Selection criteria for the $z \sim 0.7$ spectroscopic sample (quiescent galaxies in red, star-forming galaxies in blue) relative to $0.4 < z_{phot} < 0.95$ galaxies in the NMBS-COSMOS field. Filled circles represent successful measurements of velocity dispersions (with <15% statistical error), and crosses represent galaxies with spectra that have been excluded from this sample, as a result of either failed extraction or insufficient S/N. (a) $U-V$ rest-frame color vs. inferred velocity dispersion: galaxies are selected to span a range in both quantities. (b) $U-V$ vs. $V-J$ rest-frame colors, used to distinguish between star-forming (lower right of solid black dividing lines, indicating Whitaker et al. (2012) empirical distinctions) and quiescent galaxies (upper left).

to the σ selection, targets were selected within $0.4 \lesssim z_{phot} \lesssim 1$ and brighter than $I = 23.5$. Priority was given to spanning the observed range of $U-V$ color, inferred velocity dispersion, Sérsic index, and star formation rate. Finally, additional low-mass ($\sigma \lesssim 100$ km s^{-1}) galaxies within the same redshift range were added to fill spectroscopic masks. These filler galaxies are apparent at the low-σ end of Figure 1(a) (and later in Figure 4(f)) and were biased toward brighter (and bluer) galaxies.

In some cases (13 galaxies), we failed to successfully extract a sufficient 1D spectrum for one or both of the red and blue chips; these spectra are excluded from the final sample. The remaining 148 galaxies are included in this work.

2.3. Imaging and Photometric Catalogs

Stellar population analysis and rest-frame color estimates for galaxies in this sample are based on multiwavelength broad- and medium-band photometric data from two fields: the UKIDSS-UDS and NMBS-COSMOS. Additionally, high-resolution, space-based imaging taken using the Advanced Camera for Surveys (ACS) and the Wide Field Camera 3 (WFC3) on the *Hubble Space Telescope* (*HST*) exists in both fields, also described in Section 2.4.

In the COSMOS field, we utilize v5.1 NMBS catalogs, which we briefly summarize below; see Whitaker et al. (2011) for a full description. This data set is designed around deep medium-band near-infrared (NIR) imaging in $J1$, $J2$, $J3$, $H1$, $H2$ bands from the Mayall 4.0 m telescope in addition to a multitude of ancillary data. Optical imaging is included from the Deep Canada–France–Hawaii Telescope Legacy Survey (Erben et al. 2009; Hildebrandt et al. 2009) (u', g', r', i', z') and deep Subaru imaging in B_J, V_J, r^+, i^+, z^+ and 12 medium-band optical filters (Taniguchi et al. 2007). Ultraviolet data are included in the near-UV and far-UV from the *Galaxy Evolution Explorer* (*GALEX* Martin et al. 2005). Additional IR measurements are included in the NIR from the WIRcam Deep Survey (Bielby et al. 2012) (J, H, K) and in the four mid-IR channels of *Spitzer*-IRAC data and *Spitzer*-MIPS 24 μm fluxes.

We utilize a K-selected v.4.1 catalog in the UKIDSS-UDS field (Williams et al. 2009). In addition to the deep NIR imaging (J, H, K) from the UKIDSS-UDS survey (Warren et al. 2007), this catalog includes optical imaging in the field from the Subaru/*XMM-Newton* Deep Survey (Furusawa et al. 2008) (U, B, V, R, i, z) and four channels of *Spitzer*-IRAC data.

2.4. Derived Properties: Sérsic Profiles, Stellar Populations, and Rest-frame Colors

Galaxy morphologies are measured by fitting 2D Sérsic models using GALFIT (Peng et al. 2002) to *HST* imaging, either from CANDELS F160W WFC3 imaging (van der Wel et al. 2012) when available (74 galaxies) or from ACS F814W imaging (Bezanson et al. 2011) in NMBS-COSMOS (59 galaxies). Figure 2 includes galleries of $9'' \times 9''$ cutouts of quiescent and star-forming galaxies, from either CANDELS v1.0 mosaics (Grogin et al. 2011; Koekemoer et al. 2011) or COSMOS ACS v2.0 mosaics (Koekemoer et al. 2007; Massey et al. 2010). Quoted sizes are circularized such that $r_e = \sqrt{ab}$, where a and b are the semimajor and semiminor axes, respectively, of the half-light ellipse. Errors in size estimates are assumed to be ~10% when not quoted. We exclude 15 galaxies with only ground-based sizes for this work.

Utilizing the excellent spectral coverage of the photometric data in each field, we use FAST (Kriek et al. 2009) to fit the spectral energy distribution of each galaxy to Bruzual & Charlot (2003, BC03) stellar population synthesis models, assuming solar metallicity, a Chabrier (2003) initial mass function, and delayed exponential declining star formation histories. We assume the best-fit parameters, such as stellar mass, age, and A_v, from these fits. We adopt a systematic uncertainty in measured $M_\star/L$ of 0.1 dex, although we note that in some cases the systematic uncertainties in such measurements could be up

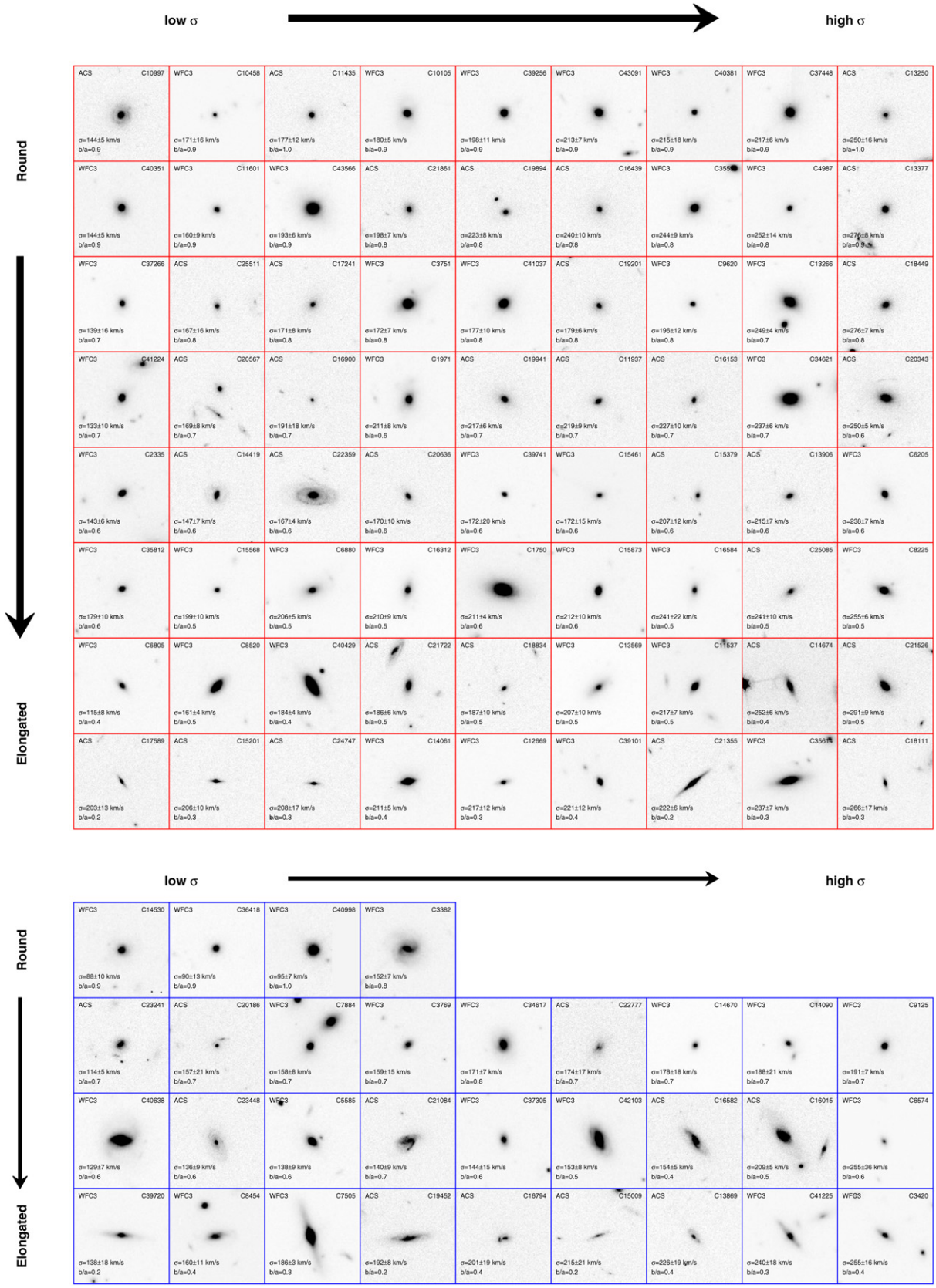

Figure 2. Images of quiescent (top panels with red outlines) and star-forming (bottom panels with blue outlines) galaxies, ordered by axis ratio (vertical) and velocity dispersion (horizontal). Images are $9'' \times 9''$ and are taken from mosaic images of the COSMOS and UDS fields. Images labeled (left upper corner) WFC3 are extracted from CANDELS v1.0 F160W mosaics (Grogin et al. 2011; Koekemoer et al. 2011) and labeled ACS are from COSMOS v2.0 ACS mosaics (Koekemoer et al. 2007; Massey et al. 2010). Galaxy IDs are indicated in the upper right corner of each panel.

to ∼0.2 dex (e.g., Muzzin et al. 2009). Because these stellar mass estimates are based on aperture photometry, corrected by some average aperture-to-total magnitude correction, we rescale stellar masses to reflect the luminosity of the best-fit Sérsic profile as

$$M_\star = M/L_{\star,\mathrm{FAST}} L_{\mathrm{Tot}}. \quad (7)$$

In this equation, $M_\star$ is the corrected stellar mass, $M/L_{\star,\mathrm{FAST}}$ is the stellar mass-to-light ratio estimate from FAST, and L_{Tot} is the total luminosity of the best-fit Sérsic profile.

Additionally, we use InterRest (Taylor et al. 2009) to interpolate between observed photometric measurements for each galaxy and calculate rest-frame magnitudes and colors in a number of filters.

2.5. Velocity Dispersion Measurements

Velocity dispersions of stellar absorption features were measured using the Penalized Pixel-fitting (pPXF) Software (Cappellari & Emsellem 2004) to fit broadened Bruzual & Charlot (2003) (BC03) stellar population synthesis models to each spectrum. Possible emission lines (e.g., O II and O III lines) were excluded from dispersion fitting, and spectral regions surrounding the Balmer lines were masked. In order to limit the effect of template mismatch on measured velocity dispersions, we used the best-fit synthetic spectrum to the photometry as determined by FAST (Kriek et al. 2009) and fit only rest-frame $\lambda > 4000$ Å to avoid age-dependent features such as strong Balmer lines (see, e.g., van de Sande et al. 2013). All velocity dispersions were visually inspected, and errors were estimated by refitting templates added to shuffled residuals from initial fits using pPXF. Spectra and broadened BC03 templates are included in Figure 3, ordered by measured velocity dispersion. We compare these error estimates to statistical errors in velocity dispersion calculated by pPXF and verify that they are extremely consistent, with a scatter in relative error of only 0.01.

Measured velocity dispersions are corrected (by adding in quadrature) for the BC03 template resolution, $\sigma = 85\,\mathrm{km\,s^{-1}}$. Velocity dispersions are then aperture corrected using Equation (1) from the 1″ slit width to an effective radius. Galaxies with ⩾15% velocity dispersion errors are excluded from the final sample (30 galaxies, 12 quiescent, and 18 star-forming), yielding a full sample of 103 galaxies spanning a range of colors and velocity dispersions (see Table 1).

2.6. Sample Completeness: Measurement Success Rates for Absorption-line Kinematics

This sample of galaxies was selected to span the population of massive ($\sigma \gtrsim 100\,\mathrm{km\,s^{-1}}$) galaxies at $z \sim 0.7$ and therefore the range in stellar populations (or colors), masses, morphologies, and dynamics. Derived properties of the final spectroscopic sample are included in Table 1. In Figure 4 we assess the range of the final spectroscopic sample relative to galaxies in the same (photometric) redshift range from the NMBS-COSMOS field (parent population). The parent population is indicated by small gray dots; the spectroscopic sample is indicated by colored symbols. Our goal is to represent both star-forming and quiescent galaxy populations in this analysis. We distinguish between the two samples using rest-frame $U-V$ and $V-J$ colors (e.g., Franx et al. 2008; Williams et al. 2009), adopting the color cuts from Whitaker et al. (2012; Figure 1). This method has been shown to discriminate between "red and dead" galaxies and galaxies that are red and dusty star formers. In this and subsequent figures, star-forming galaxies are indicated by blue symbols and quiescent galaxies by red symbols.

For some spectra, we were not able to successfully measure velocity dispersions (indicated by crosses). This is driven partially by S/N of the spectra: these failures appear to be related to a number of correlated galaxy properties. Therefore, the resulting sample of galaxies does not uniformly sample colors, morphologies, and dynamics as described in Section 2.2. In general, star-forming galaxies are more likely to "fail" in this context.

The primary factor in failing to measure a velocity dispersion is the observed brightness of the galaxy: faint ($I \gtrsim 22$) galaxies are excluded because they are either intrinsically faint or at the highest-redshift end of this survey (Figures 4(a)–(c)). Furthermore, low-mass galaxies, as defined based on stellar mass ($\log M_\star \lesssim 10.5$) or inferred dynamics ($\sigma_{\mathrm{inf}} \lesssim 100$–$150\,\mathrm{km\,s^{-1}}$), are less likely to yield precise velocity dispersions, particularly those included as mask fillers. A total of 75% of failed measurements of quiescent galaxies, and ∼40% for star-forming galaxies, have $\sigma_{\mathrm{inf}} < 100\,\mathrm{km\,s^{-1}}$; therefore, the sample is much more complete above this limit. Blue star-forming galaxies are also more likely to fail, although this is partially related to the mass bias. Additionally, this sample excludes many galaxies with the highest specific star formation rates (see Figure 4(f)). This can be understood as a combination of the aforementioned mass bias against low velocity dispersions and the fact that the youngest stellar population synthesis models have quite weak spectral absorption features (aside from the Balmer lines, which are masked in the dynamical fitting).

Although the existing sample spans a large range in morphologies and inclinations (see images in Figure 2), there also appears to be a bias against face-on disks as many galaxies with rounder shapes ($b/a \gtrsim 0.8$ in Figure 4(d)) and more disk-like profiles (Sérsic $n \lesssim 2.5$ in Figure 4(e)) preferentially fail to produce successful dispersion measurements. For galaxies with rotation, such as inclined *pure* disks, the measured velocity dispersion is a combination of the rotational velocity and intrinsic velocity dispersion. Weiner et al. (2006a) found that the measured integrated (1D) velocity dispersion is well approximated by the quantity $S_{0.5}$, which is defined as

$$S_{0.5}^2 = 0.5 V_{\mathrm{rot}}^2 + \sigma_{2D}^2, \quad (8)$$

where V_{rot} is the inclination-corrected velocity dispersion. For a face-on inclination ($i = 0$), the rotational velocity does not contribute at all to the measured velocity dispersion. For inclined galaxies, measured dispersions will be boosted by the rotational velocities (by broadening the spectral features), which in turn makes them more likely to be included in the spectroscopic sample. The velocity dispersion of an edge-on disk galaxy provides an estimate of the overall dynamics of the galaxy, but just the intrinsic dispersion for a face-on galaxy. Inclination, as probed by projected axis ratios, appears to have a minimal effect on the samples of galaxies presented in this paper, implying that intrinsic dispersions are high and possibly pointing to the prevalence of bulges in these massive galaxies (see Appendix A).

Overall this sample is representative for massive galaxies at $z \sim 0.7$, but the results of the study will not be as comprehensive for lower-mass galaxies or galaxies with high star formation rates. The former is driven primarily by S/N: deeper data would provide higher completeness to lower mass limits. The latter is a limitation to studying absorption-line kinematics for very young systems.

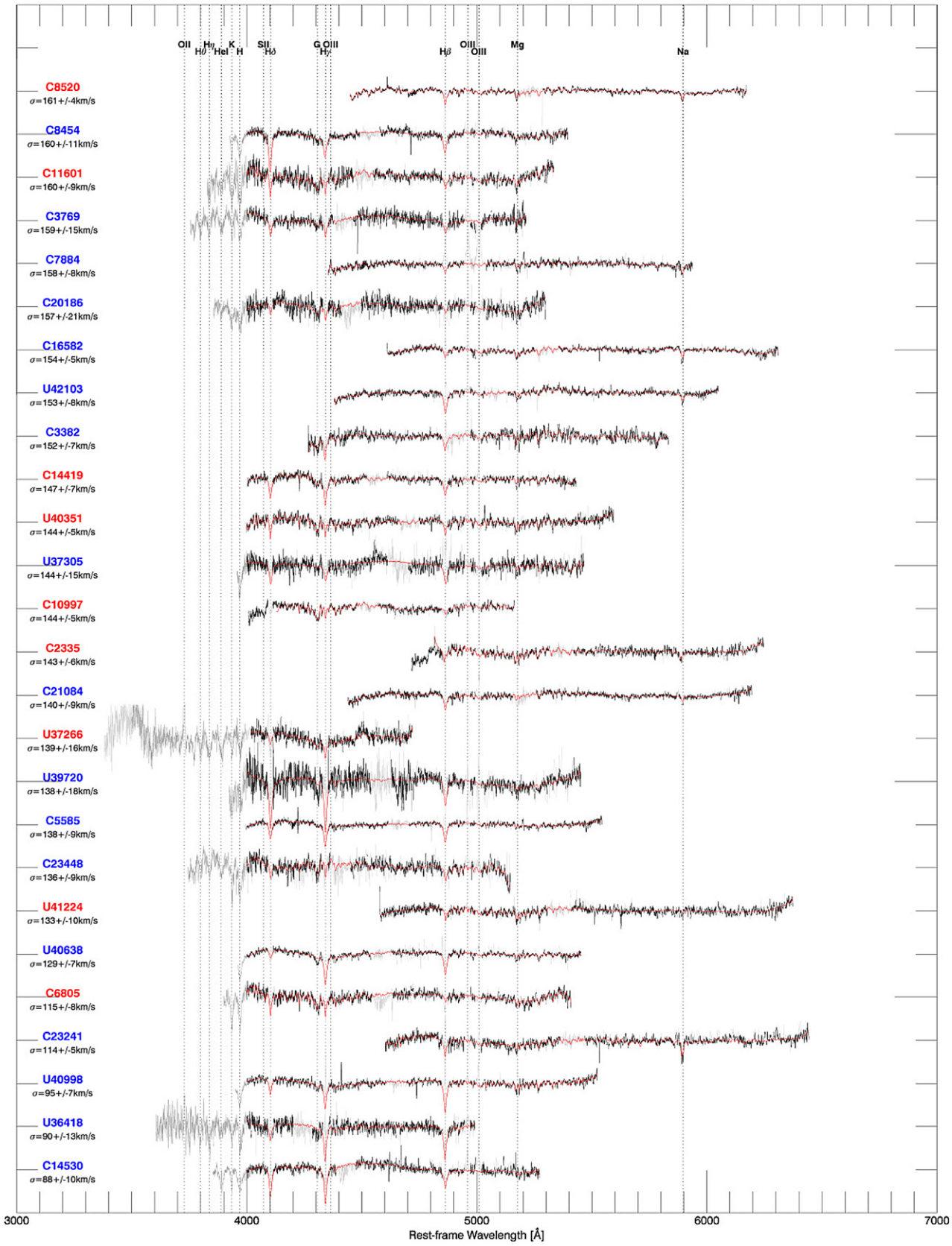

Figure 3. Continuum-normalized galaxy spectra, ordered by velocity dispersion and shifted to rest-frame wavelengths. Full spectra are included in gray, regions of the spectra that are included in the dynamical measurements are included in black ($\lambda > 4000$ Å), and broadened best-fit BC03 templates are red. Key spectral features are labeled at the top of each panel and indicated by dashed vertical lines. Galaxy IDs are labeled to the left of each spectrum, with the color of the label indicating whether a galaxy is star-forming (blue) or quiescent (red). DEIMOS spectra of $z \sim 0.7$ galaxies, ordered by velocity dispersion.

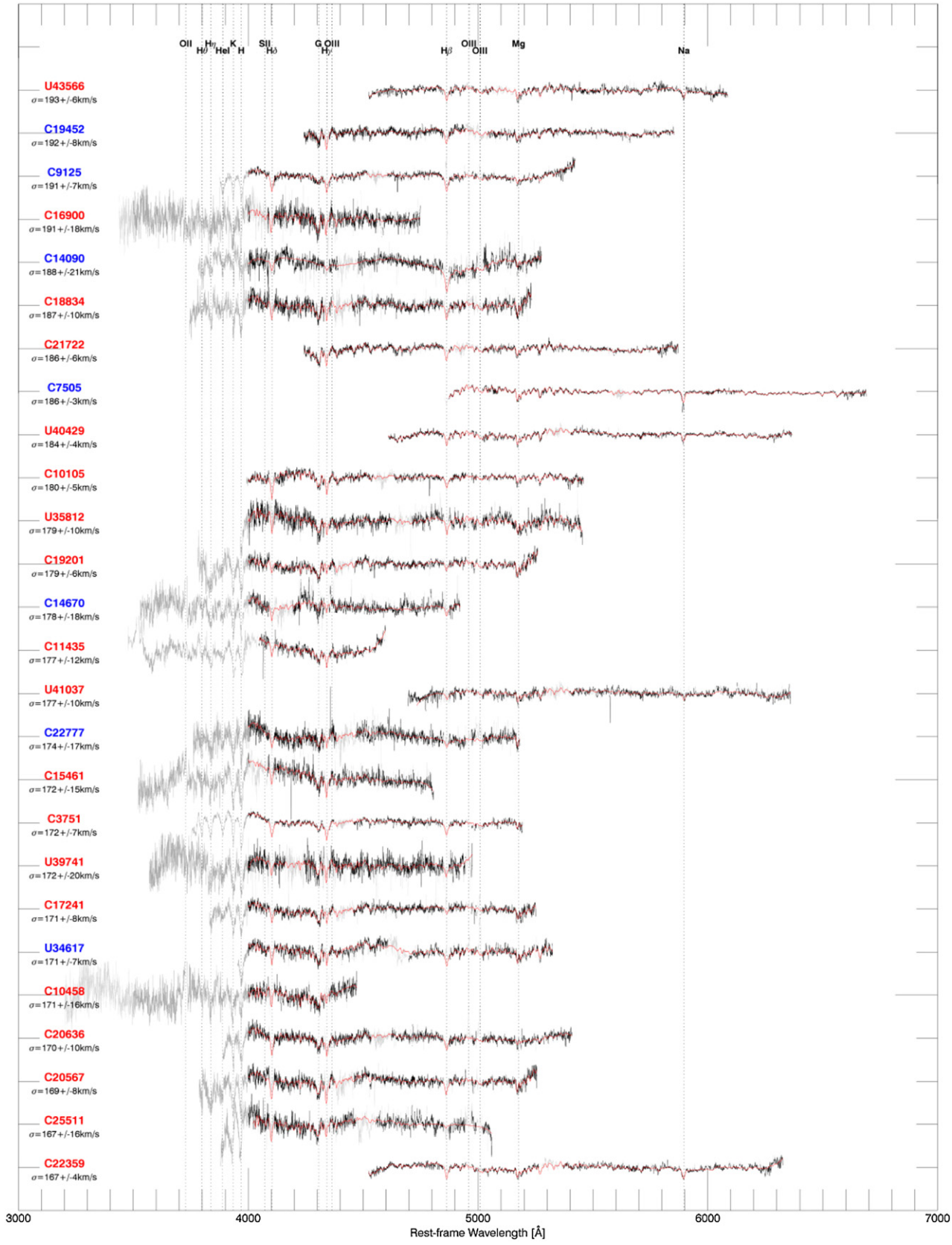

Figure 3. (Continued)

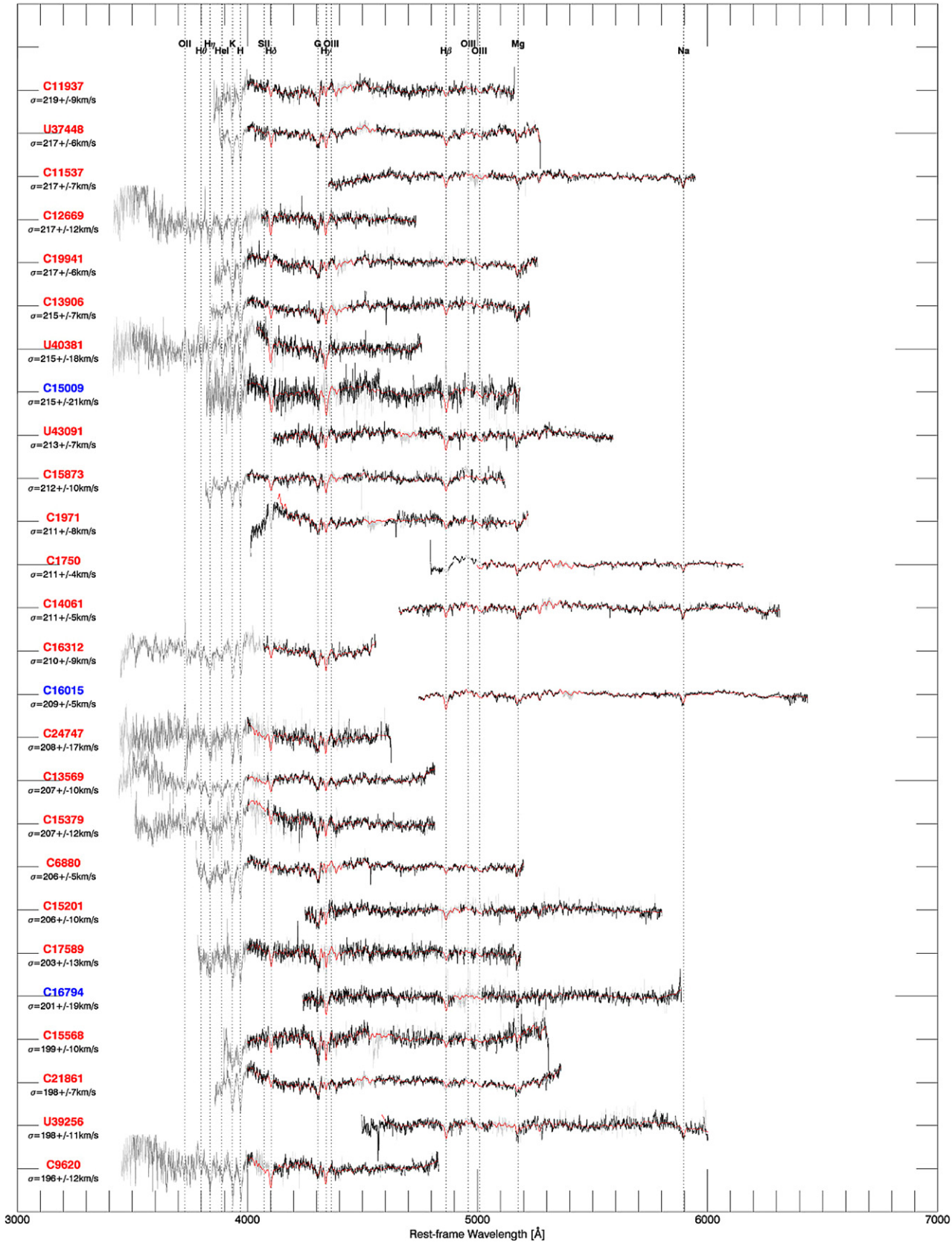

Figure 3. (Continued)

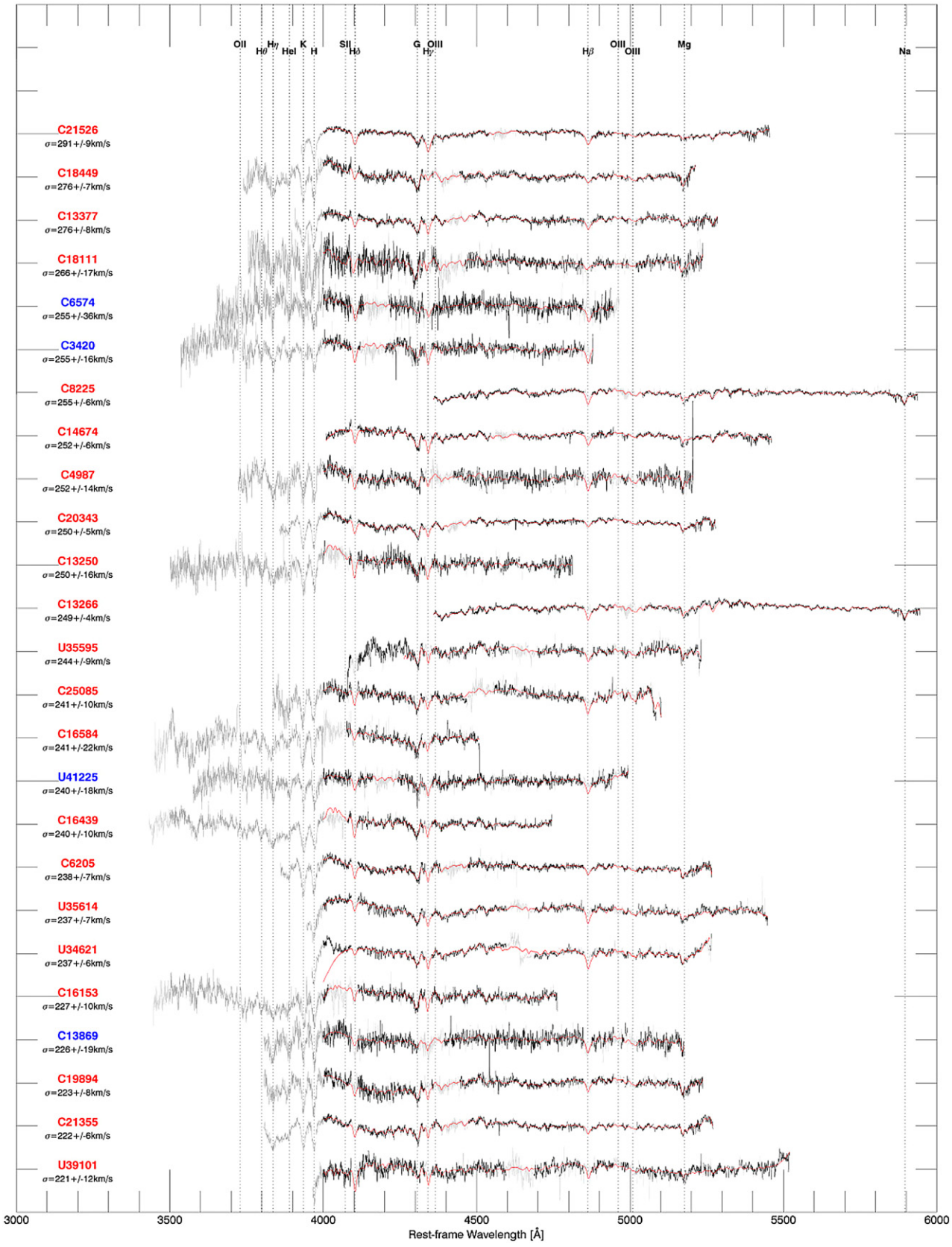

Figure 3. (Continued)

Table 1
DEIMOS $z \sim 0.7$ Sample—Galaxy Properties

Id	R.A. (^{o})	Decl. (^{o})	z	R_e (kpc)	n	Filter	log Stellar Mass ($M_\odot$)	$\sigma_{\rm aperture}$ (km s^{-1})	$\sigma_{\rm Re}$ (km s^{-1})	Exposure Time (s)
C1971	150.104	2.198	0.682	4.4	4.7	WFC3-F160W	10.96	214 ± 8	211 ± 8	49200
C2335	150.097	2.205	0.424	0.8	2.7	WFC3-F160W	10.13	131 ± 5	143 ± 6	49200
C3382	150.084	2.222	0.560	5.9	1.5	WFC3-F160W	10.62	158 ± 7	152 ± 7	49200
C3420	150.119	2.223	0.839	2.1	3.3	WFC3-F160W	10.83	245 ± 15	255 ± 16	49200
C3751	150.121	2.227	0.733	3.6	2.9	WFC3-F160W	11.07	171 ± 7	172 ± 7	49200
C3769	150.121	2.230	0.732	2.0	0.8	WFC3-F160W	10.10	153 ± 14	159 ± 15	49200
C4987	150.116	2.250	0.747	1.4	4.2	WFC3-F160W	10.47	236 ± 13	252 ± 14	49200
C5585	150.104	2.261	0.642	1.9	1.7	WFC3-F160W	10.15	133 ± 9	138 ± 9	49200
C6205	150.086	2.272	0.728	1.5	4.7	WFC3-F160W	10.65	225 ± 6	238 ± 7	49200
C6574	150.083	2.278	0.835	1.6	1.8	WFC3-F160W	10.49	241 ± 34	255 ± 36	49200

(This table is available in its entirety in machine-readable form.)

3. THE DISCREPANT STRUCTURAL AND DYNAMICAL PROPERTIES OF STAR-FORMING AND QUIESCENT GALAXIES

In this section we focus on two traditional scaling relations (size–mass and mass–velocity dispersion, or the mass Faber–Jackson, relation) to highlight the differences between star-forming and quiescent galaxies, at both $z \sim 0$ and $z \sim 0.7$. These relations are non-edge-on projections of the mass fundamental plane, which is the focus of subsequent sections. Although the populations are distinguished based on their rest-frame colors, as a proxy for differences in stellar populations, the separation extends to the overall structural and dynamical properties of each sample of galaxies in this paper.

In Figure 5 we explore the size–mass relations of the star-forming and quiescent galaxies in the SDSS and at $z \sim 0.7$. In Figure 5(a), as in the subsequent $z \sim 0$ figures in this paper, the distribution of galaxies in the SDSS is demarcated by a series of contours. Red contours indicate the density of quiescent

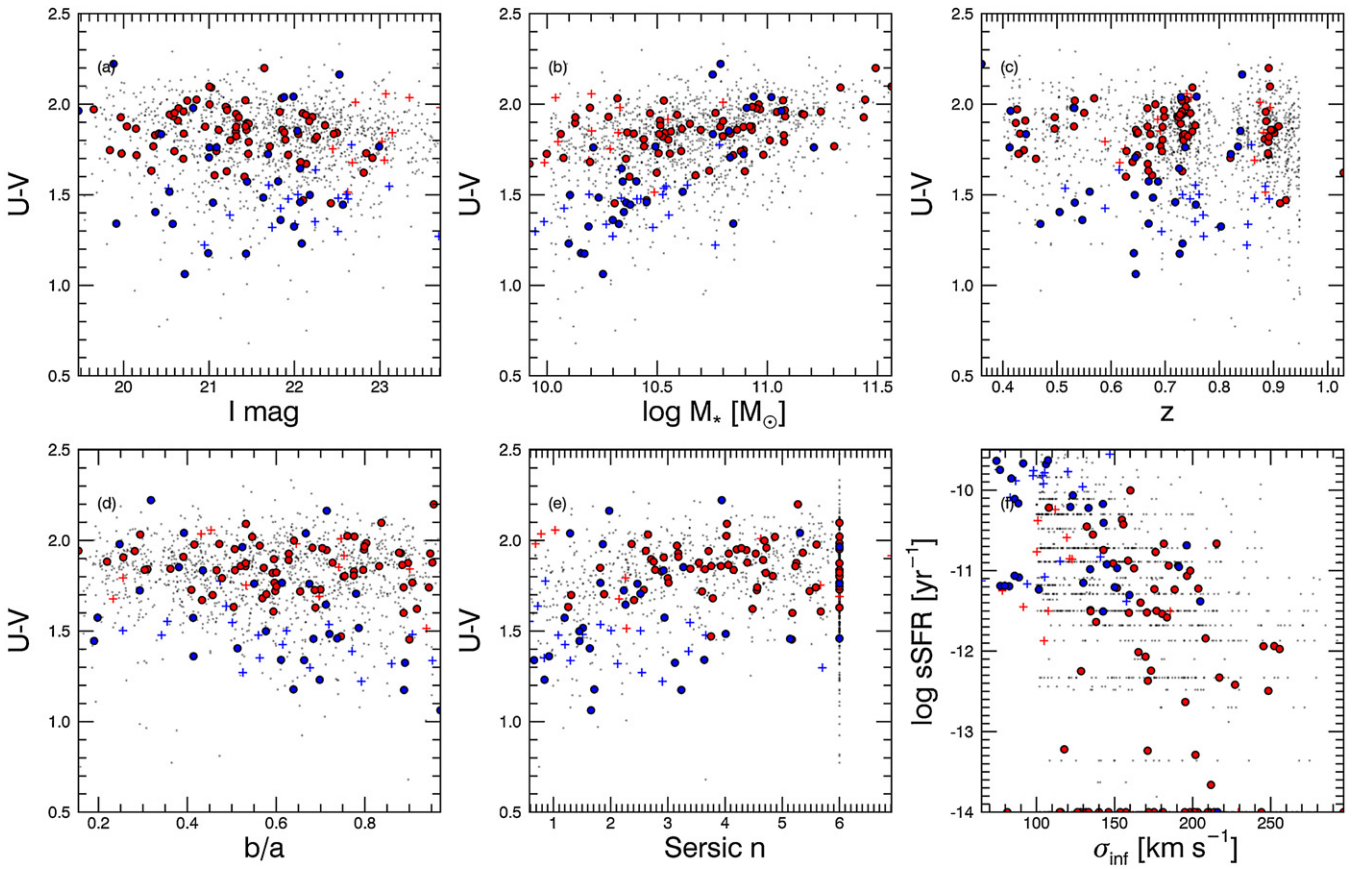

Figure 4. Properties of the $z \sim 0.7$ spectroscopic sample (quiescent galaxies in red, star-forming galaxies in blue) relative to $0.4 < z_{\rm phot} < 0.95$ galaxies in the NMBS-COSMOS field. As in Figure 1, filled circles represent successful measurements of velocity dispersions (with <15% statistical error), and crosses represent galaxies with spectra that have been excluded from this sample. Blue symbols identify star-forming galaxies, and red symbols represent quiescent galaxies, separated using rest-frame $U-V$ and $V-J$ colors. The spectroscopic sample spans the range of the photometric parent sample in $U-V$ color (panels (a)–(e)), I magnitude (panel (a)), stellar mass (panel (b)), axis ratio (panel (d)), Sérsic index (panel (e)), specific star formation rate, and inferred velocity dispersion (panel (f)). However, at the extremes of the sample (e.g., at high redshift or low mass), the spectroscopic sample is biased relative to a full mass-limited photometric sample.

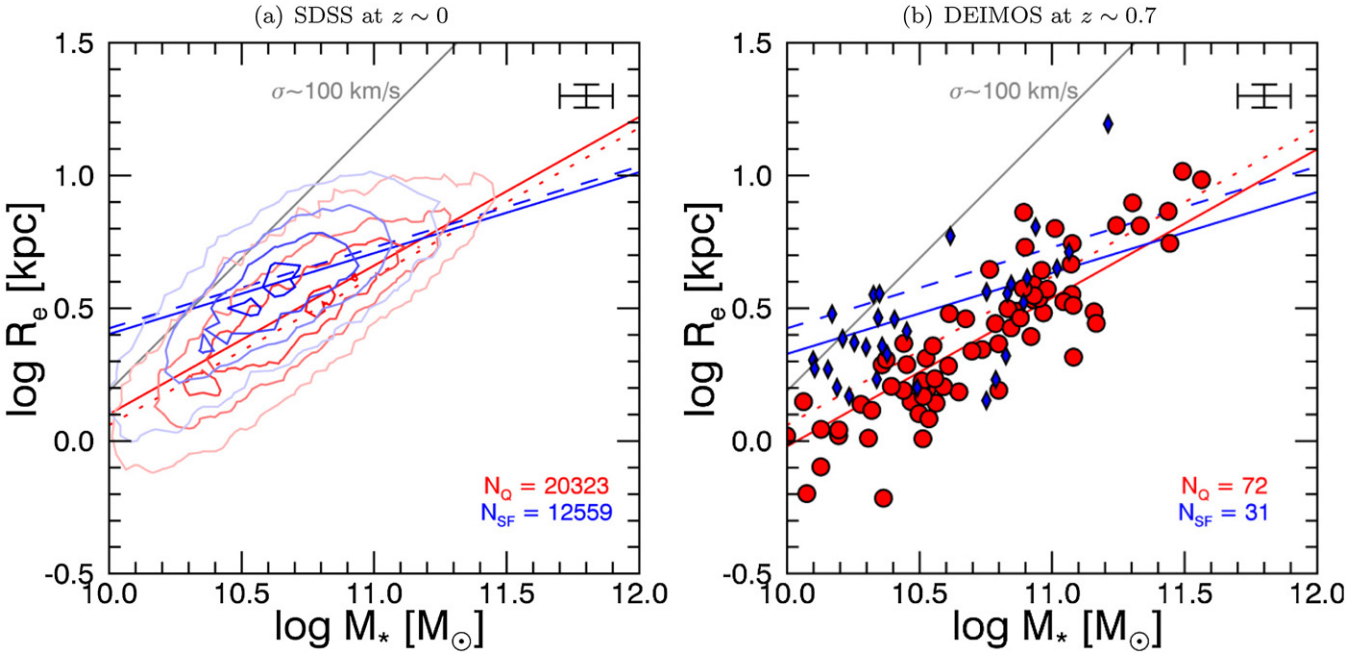

Figure 5. Circularized effective radius vs. stellar mass for all galaxies in each redshift bin. At fixed mass, star-forming galaxies have larger sizes than quiescent galaxies, at both $z \sim 0$ (panel (a), SDSS sample) and $z \sim 0.7$ (panel (b), DEIMOS sample). Total number of quiescent and star-forming galaxies is indicated in the lower right corner of each panel. Red and blue contours indicate quiescent and star-forming galaxies, respectively, based on *K*-corrected colors ($g^{0.1} - r^{0.1}$ and $M_r^{0.1}$) in panel (a). Red circles and blue diamonds indicate quiescent and star-forming galaxies, respectively, based on rest-frame $U - V$ and $V - J$ colors in panel (b). The local (Shen et al. 2003) size–mass relations are indicated for late-type (blue dashed) and early-type (red dotted) galaxies in each panel.

galaxies, and blue contours reflect the density of star-forming galaxies. The relative saturation of the colors is normalized to reflect the density in a given figure. The number of galaxies (quiescent and star-forming) is indicated by N_Q and N_{SF} in the bottom right corner of each panel. In Figure 5(b) and other $z \sim 0.7$ figures, dots represent individual galaxies. Star-forming galaxies are indicated by blue diamonds and quiescent galaxies by red circles. Again, the number of galaxies in each sample is indicated in the lower right corner of each panel. Finally, average error bars are indicated in the upper right corner of every panel.

The first result is a confirmation that star-forming galaxies are larger, on average, than quiescent galaxies at fixed mass (e.g., Shen et al. 2003, in the SDSS) and (e.g., Williams et al. 2009; van der Wel et al. 2014, at higher redshift). The discrepant normalizations for the two populations hold in both redshift ranges probed by this study. We note that the requirement of reliable velocity dispersion measurements biases this sample against galaxies with low masses and/or large sizes. Therefore, a linear fit to these size–mass relations would be steeper than for purely photometric samples of galaxies. We indicate the approximate size–mass relation of $\sigma \sim 100\,\mathrm{km\,s^{-1}}$ galaxies (gray solid line); above this line the samples likely suffer from incompleteness. Additionally, we include the Shen et al. (2003) size–mass relations for early-type (dotted red line) and late-type (dashed blue line) galaxies. By adopting the slopes of these relations, we fit the normalizations to each separate galaxy population (solid red and blue lines). We note that the overall normalizations for this sample differ from the Shen et al. (2003) fits, likely owing to the differences in (Simard et al. 2011) size measurements adopted in this work relative to the NYU-VAGC measurements (Blanton et al. 2005) used in that study. The latter measurements have been shown to underestimate galaxy sizes, by a factor that increases with Sérsic index (e.g., Guo et al. 2009). However, we include these fits mostly for relative comparisons and emphasize the importance of more complete photometric samples to properly measure the size–mass relation.

Figure 5(b) shows the same relation for massive galaxies at $z \sim 0.7$. Again, star-forming galaxies lie above quenched galaxies, and both samples lie below the Shen et al. (2003) relations; in this case this reflects the size evolution of galaxies. A comparison of Figures 5(a) to (b) shows the same thing: both star-forming and quiescent galaxy populations exhibit lower normalizations at $z \sim 0.7$ than for galaxies in the SDSS (see, e.g., van der Wel et al. 2014, for a more thorough and unbiased study of this evolution to $z \sim 3$).

In Figures 6 and 7 we present the same size–mass relations split into bins of best-fit Sérsic index to emphasize the comparison at fixed profile shape. Panel-to-panel differences suggest that the sizes of galaxies depend on Sérsic index in addition to stellar populations and stellar mass. This is particularly obvious for quenched galaxies; however, the trends in normalization do not vary linearly with Sérsic index. Instead, for galaxies in the SDSS, sizes decrease with Sérsic index for $n < 4$ and then increase with larger Sérsic indices. A similar trend exists for high-n quiescent galaxies in the $z \sim 0.7$ sample, but the sample size for star-forming and low-n galaxies is too small to assess similar trends in size with Sérsic index.

Additionally, Figure 6 demonstrates that the size difference between star-forming and quenched galaxies exists for the entire population and at fixed Sérsic index. This is particularly noteworthy and suggests, for example, that a star-forming galaxy whose profile looks like an elliptical galaxy ($n \sim 4$) will be larger than a quiescent elliptical galaxy with the same stellar mass. Although such galaxies are less common (star-forming galaxies generally have lower Sérsic indices), this suggests that the difference between star-forming and quiescent galaxies is less clear than a simple separation between disks and ellipticals.

Figure 7 demonstrates that star-forming galaxies in the $z \sim 0.7$ sample are also larger and have lower Sérsic indices

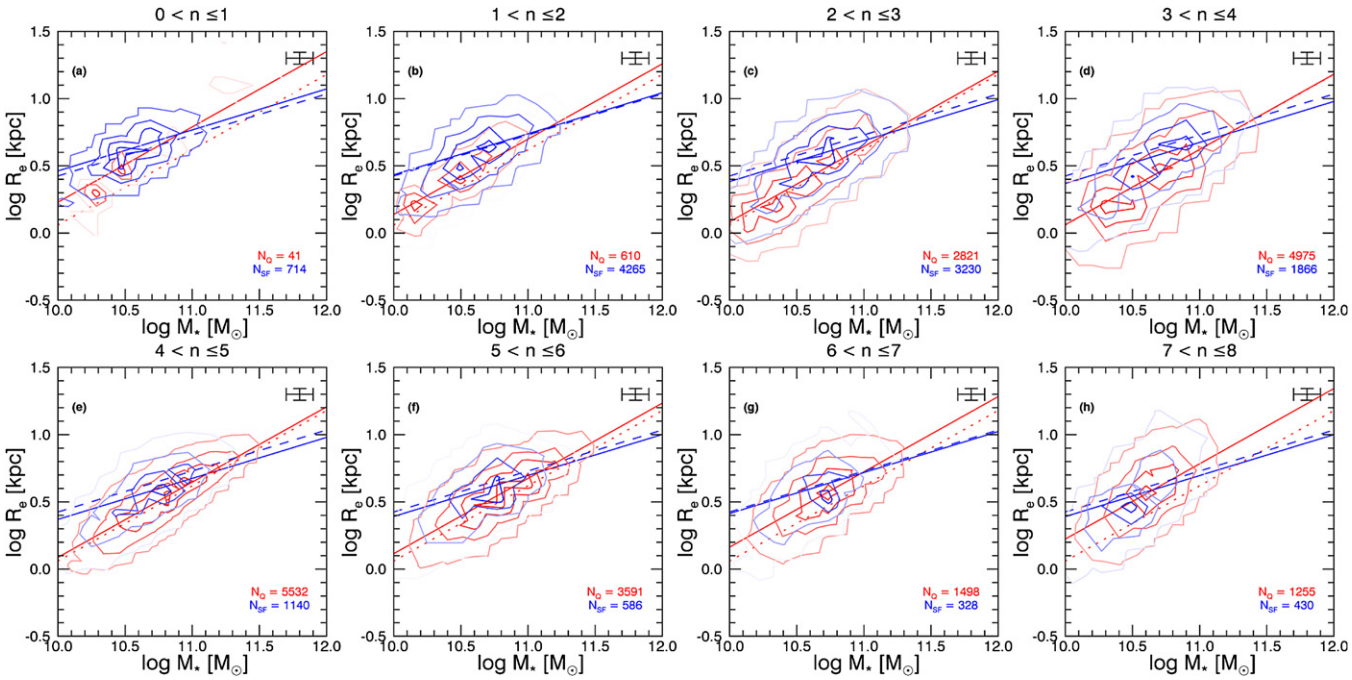

Figure 6. Circularized effective radius vs. stellar mass for galaxies in the SDSS in bins of best-fit Sérsic index (n). As in Figure 5(a), red and blue dots indicate quiescent and star-forming galaxies, respectively. The total number of quiescent and star-forming galaxies is indicated in the lower right corner of each panel (N_{SF} and N_Q). The $z \sim 0$ (Shen et al. 2003) size–mass relations are indicated for late-type (blue dashed line) and early-type (red dotted line) galaxies in each panel. This figure demonstrates that the distinction between star-forming and quiescent galaxies is not merely a cut in profile shape: at fixed mass and fixed Sérsic index, star-forming galaxies have larger sizes than quiescent galaxies. They also differ morphologically: galaxies with low Sérsic indexes tend to be star-forming, whereas those with high Sérsic indexes tend to be quenched, although this is not an exact delineation.

than their quiescent counterparts. However, the sample is quite small, so this trend at fixed Sérsic index is less pronounced, particularly at high values of n. The quiescent galaxies also suggest a similar trend of larger size with Sérsic index, but a larger, less biased sample would be better suited for measuring this effect. Finally, we emphasize that for any sample of galaxies, mass–size relations have a significant amount of scatter; individual star-forming and quiescent galaxies with exactly the same masses, sizes, and Sérsic indices are likely to exist. We caution against drawing conclusions from comparisons between small samples of galaxies.

Similarly, we compare the mass–velocity dispersion relations ("stellar mass" Faber–Jackson relation, or the Faber & Jackson (1976) relation with luminosity multiplied by $M_\star/L$) for star-forming and quiescent galaxies in the full samples (Figure 8(b)) and at fixed Sérsic index (Figures 9 and 10). This projection of the mass fundamental plane has been studied extensively, particularly for early-type galaxies; it has relatively low scatter but is not an edge-on projection of the mass fundamental plane. As discussed in Section 2.6, we use aperture-corrected velocity dispersions of star-forming galaxies in this analysis, which is a combination of intrinsic velocity dispersion, rotational velocity, and inclination (see Equation (8)). The contribution of rotational velocity to this quantity is likely to be more important for star-forming galaxies.

Best-fit slope and normalization of the mass Faber–Jackson relations (Equation (11)) for all galaxies and separately for star-forming and quiescent galaxies are reported in Table 3. These fits are calculated by an orthogonal least-squares bisector fit, which has been shown to best retrieve the underlying functional relation from astronomical data (Isobe et al. 1990) and was performed using the IDL task *SIXLIN*, with errors estimated using bootstrap resampling. The slope of the relation (A_{FJ}(SDSS) = 0.41, A_{FJ}(DEIMOS) = 0.33) for the full population of galaxies in both samples falls between the values obtained by the ATLAS-3D team (Cappellari et al. 2013a), who found that the relation has a mass dependence: $\sigma \propto M^{0.43}$ for $\sigma_{re} \lesssim 140\,\mathrm{km\,s^{-1}}$, $\sigma \propto M^{0.21}$ for larger velocity dispersions. Because the ATLAS-3D sample was composed of early-type galaxies, comparing to the slopes for the quiescent galaxy populations is more self-consistent, for which the measured slopes also (A_{FJ}(SDSS) = 0.37, A_{FJ}(DEIMOS) = 0.28) fall between the published slopes, given the selection bias toward $\sigma > 100\,\mathrm{km\,s^{-1}}$.

In the SDSS (Figure 8(a)), the velocity dispersions of quiescent galaxies are generally higher than for star-forming galaxies at fixed mass. In addition, the slope of the best-fit linear relation is slightly steeper for the full sample of star-forming galaxies. The trend in relative normalization between the two populations holds at fixed Sérsic index (Figure 9), along with overall variation in normalization with profile shape. This Sérsic dependence is especially clear for quiescent galaxies, which exhibit steeper slopes and higher normalizations (relative to the overall relation, indicated by a dashed black line) with increasing n. Star-forming galaxies with $n \gtrsim 1$ exhibit a weaker trend of increasing normalization and increasing slope with Sérsic index.

Figure 8(b) demonstrates that velocity dispersions are also lower for star-forming galaxies relative to quiescent galaxies in the $z \sim 0.7$ sample. The normalization of this relation is offset with respect to the $z \sim 0$ relation such that dispersions are higher with redshift. Recently, van de Sande et al. (2013) and Belli et al. (2014a) presented a similar trend for samples of quiescent galaxies at $z \sim 2$ and $z \sim 1.2$, respectively; here

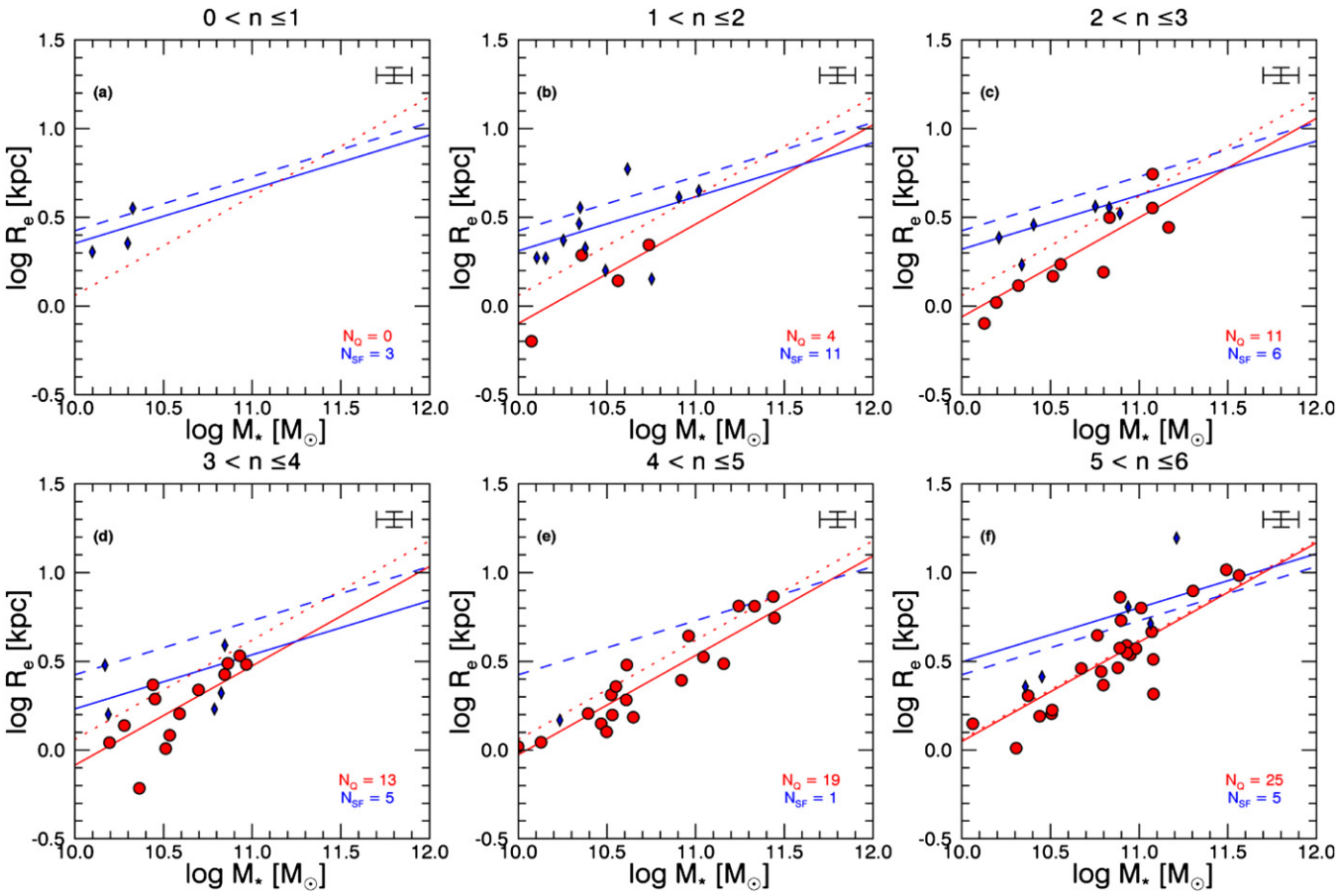

Figure 7. Circularized effective radius vs. stellar mass for galaxies in the DEIMOS sample at $z \sim 0.7$ in bins of Sérsic index (color-coding as in Figure 5(b)). The $z \sim 0$ (Shen et al. 2003) size–mass relations are indicated for late-type (blue dashed line) and early-type (red dotted line) galaxies in each panel. As at lower redshift, star-forming galaxies are generally larger and have lower Sérsic indices than quiescent galaxies at fixed mass; however, the mass–size relations for each population exhibit a large scatter (and therefore larger samples are required to quantify the relations).

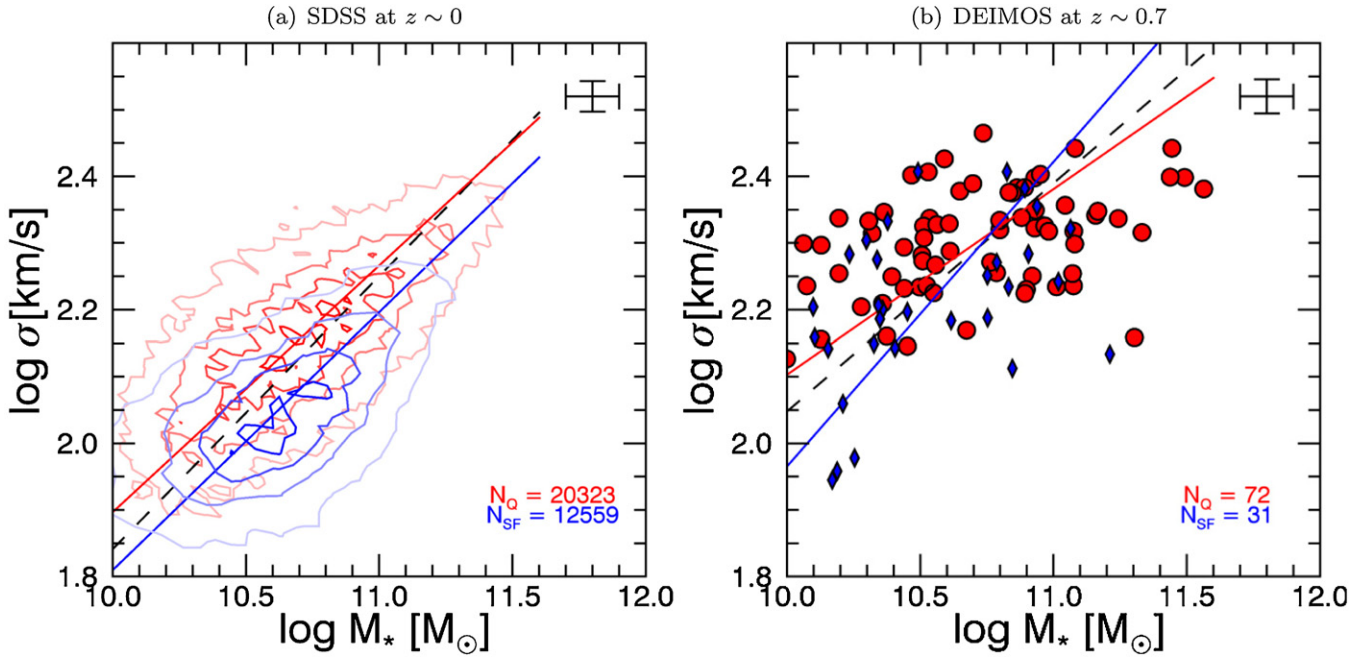

Figure 8. Velocity dispersion vs. stellar mass ("mass Faber–Jackson" relation) for all galaxies at $z \sim 0$ (panel (a)) and $z \sim 0.7$ (panel (b)) (notations and color-coding as in Figure 5). Linear fits are included as solid lines for the overall population (black) and separately for star-forming (blue) and quiescent (red) galaxies. At fixed mass, star-forming galaxies have lower velocity dispersions, at each redshift, although the slope of the relation is slightly steeper for star-forming galaxies.

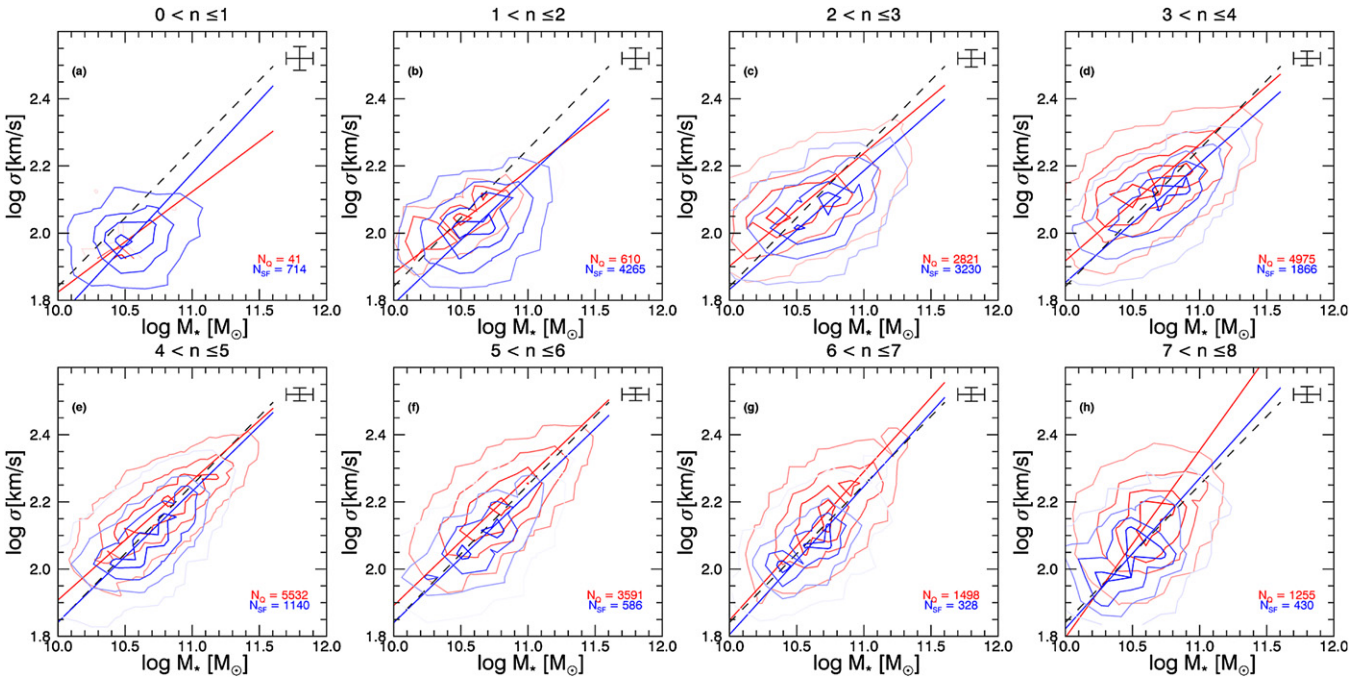

Figure 9. Stellar mass Faber–Jackson relation (velocity dispersion vs. stellar mass) for galaxies in the SDSS, split by Sérsic index (labeled as in Figures 5(a) and 9). Overall fit (from Figure 8(a)) is included as the dashed black line; fits to star-forming (blue) and quiescent (red) galaxies at fixed Sérsic index are shown as solid lines. At fixed mass and Sérsic index, star-forming and quiescent galaxies lie on different scaling relations; however, these relations also vary with n. Generally, the normalization of the mass Faber–Jackson relation is lower for star-forming galaxies than for quenched galaxies, and the slope of these relations increases with Sérsic n.

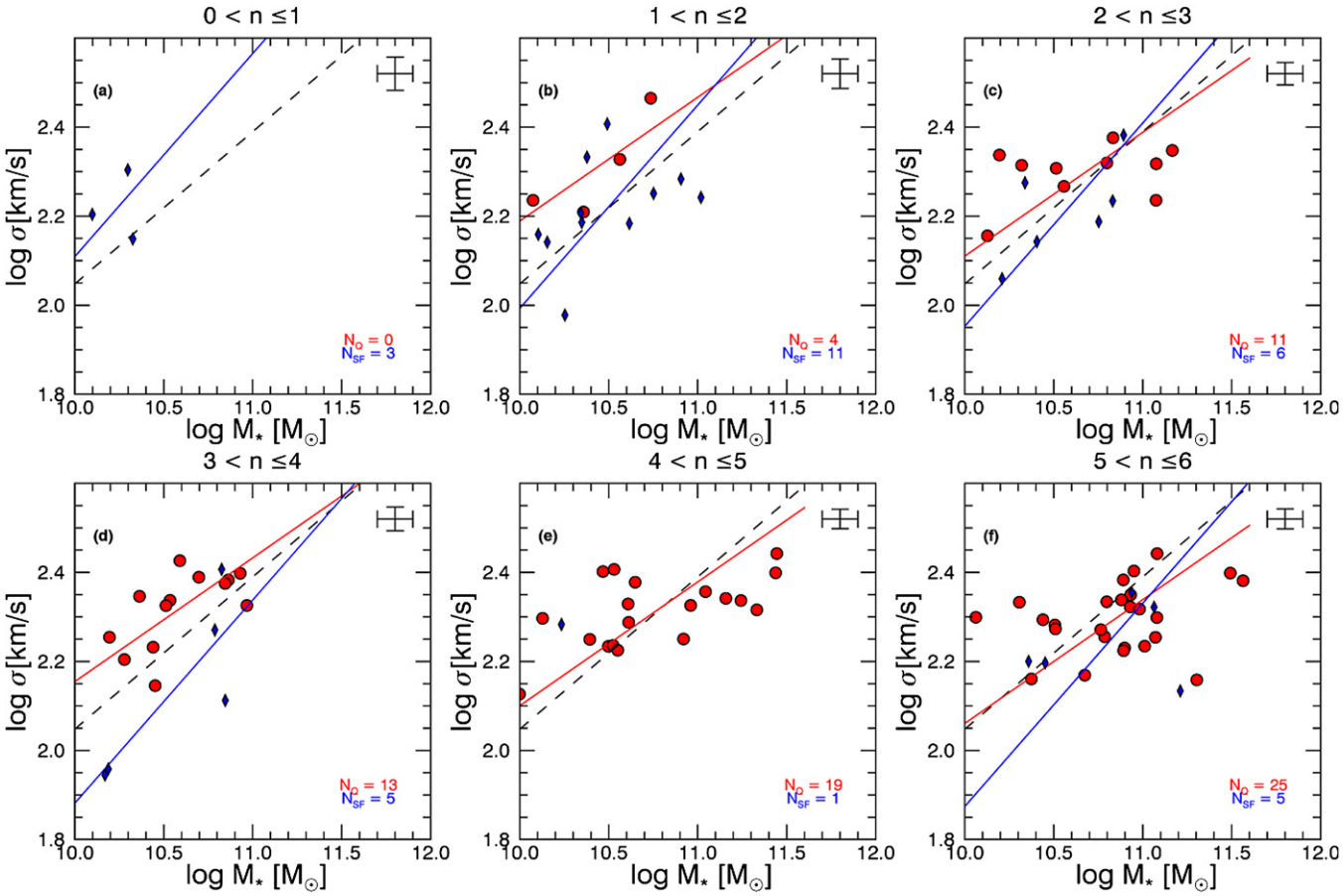

Figure 10. Stellar mass Faber–Jackson relation for galaxies in the DEIMOS sample at $z \sim 0.7$ (see also Figure 9 at $z \sim 0$). In each panel the overall mass Faber–Jackson relation at this redshift is included (black dashed line), in addition to fits to the star-forming and quiescent galaxy samples, assuming the slopes from Figure 8(b). Star-forming galaxies generally have lower velocity dispersions than their quiescent counterparts.

we note that the result seems to hold for star-forming galaxies as well.

As in Figure 7, the statistical power of this sample of galaxies breaks down at fixed Sérsic index (Figure 10). We include fits in the two galaxy samples in each panel to guide the eye, assuming the slopes measured from the full subsamples (in Figure 8(b)). Although the samples are small, we note that, if anything, the normalizations of the mass Faber–Jackson relation decrease with Sérsic index, exhibiting the opposite trend relative to the low-z sample of galaxies. However, we reiterate the need for larger samples to assess this trend robustly.

By comparing star-forming and quiescent galaxy populations in these 2D projections of the mass fundamental plane in this section, we emphasize the overall bimodality of the populations of galaxies separated initially based on their stellar populations. From this perspective, the structures (in both size and light profile), stellar dynamics (as measured by absorption-line kinematics), and scaling relations between these properties should be treated separately. This would be important for the empirical measurement of galaxy scaling relations and for the theoretical study of the formation and evolution of galaxies that are constrained to follow those relations.

4. STAR-FORMING AND QUIESCENT GALAXIES LIE ON THE SAME MASS FUNDAMENTAL PLANE

In contrast with the previous section, we turn our focus to the potential similarity between star-forming and quiescent galaxy populations. Specifically, we present the existence of a mass fundamental plane for star-forming and quiescent galaxy populations alike. The mass fundamental plane is the plane in 3D space between galaxy size (effective radius, R_e), velocity dispersion (σ), and stellar mass surface density ($\Sigma_\star \equiv (M_\star/2\pi\ R_e^2)$) (e.g., Hyde & Bernardi 2009; Bezanson et al. 2013). This plane represents a combination of the two 2D scaling relations investigated in the previous section.

Figure 11 shows an edge-on projection of the mass fundamental plane at $z \sim 0$ and $z \sim 0.7$ for star-forming and quiescent galaxies; Figures 12 and 13 show the mass fundamental plane separated by Sérsic index at each redshift. Although star-forming and quiescent galaxies are discrepant in size and velocity dispersion at fixed mass, Figure 11 demonstrates that the two populations occupy different regions of the same plane. The mass fundamental plane can be written as

$$\log R_e = \alpha \log \sigma + \beta \log \Sigma_\star + \gamma. \quad (9)$$

At $z \sim 0$, we adopt the tilt of the mass fundamental plane from Hyde & Bernardi (2009; $[\alpha, \beta] = [1.629, -0.840]$), as measured from a similar sample of galaxies in the SDSS and allow the normalization (γ) of the mass fundamental plane to vary for each sample. There is some conflicting evidence in the literature regarding the evolution of the slope of the (luminosity) fundamental plane. Holden et al. (2010) demonstrated that there is no evidence for evolution in the tilt since $z \sim 1$; however, with a larger sample of cluster data, Jørgensen & Chiboucas (2013) found evidence of evolution in both slope and normalization of the plane with redshift. Fitting the exact functional form of the fundamental plane is an extremely difficult problem, as it requires careful modeling of sample selection effects, correlated observational errors, and intrinsic scatter (e.g., Jorgensen et al. 1996), and is beyond the scope of this paper. Therefore, we assume that the Hyde & Bernardi (2009) tilt of the mass fundamental plane also applies at higher redshifts, again allowing the normalization to vary.

Table 2
Mass Fundamental Plane Normalizations

Sample	Sérsic Range	γ	γ_Q	γ_{SF}
SDSS	All	4.496 ± 0.001	4.471 ± 0.001	4.537 ± 0.001
SDSS	$0 < n \leqslant 1$	4.558 ± 0.005	4.580 ± 0.021	4.557 ± 0.005
SDSS	$1 < n \leqslant 2$	4.556 ± 0.002	4.550 ± 0.004	4.557 ± 0.002
SDSS	$2 < n \leqslant 3$	4.537 ± 0.001	4.523 ± 0.002	4.549 ± 0.002
SDSS	$3 < n \leqslant 4$	4.501 ± 0.001	4.493 ± 0.001	4.524 ± 0.003
SDSS	$4 < n \leqslant 5$	4.475 ± 0.001	4.470 ± 0.001	4.504 ± 0.003
SDSS	$5 < n \leqslant 6$	4.449 ± 0.002	4.442 ± 0.002	4.496 ± 0.005
SDSS	$6 < n \leqslant 7$	4.434 ± 0.003	4.423 ± 0.003	4.484 ± 0.008
SDSS	$7 < n \leqslant 8$	4.396 ± 0.004	4.370 ± 0.004	4.470 ± 0.010
DEIMOS	all	4.306 ± 0.015	4.321 ± 0.017	4.270 ± 0.032
DEIMOS	$0 < n \leqslant 1$	4.042 ± 0.033	4.321 ± 0.017	4.042 ± 0.034
DEIMOS	$1 < n \leqslant 2$	4.239 ± 0.044	4.232 ± 0.045	4.241 ± 0.058
DEIMOS	$2 < n \leqslant 3$	4.321 ± 0.037	4.336 ± 0.052	4.295 ± 0.037
DEIMOS	$3 < n \leqslant 4$	4.333 ± 0.031	4.280 ± 0.025	4.470 ± 0.047
DEIMOS	$4 < n \leqslant 5$	4.317 ± 0.034	4.329 ± 0.034	4.092 ± 0.000
DEIMOS	$5 < n \leqslant 6$	4.333 ± 0.026	4.344 ± 0.029	4.279 ± 0.055

Notes. Best-fit normalizations to the mass fundamental plane (see Equation (9)). The tilt of the mass fundamental plane is fixed as $[\alpha, \beta] = [1.629, -0.840]$ (Hyde & Bernardi 2009).

We verified that the assumption of a nonevolving tilt does not significantly bias any of our results as follows. First, we performed a simple fit of slope of the mass fundamental plane to the full $z \sim 0.7$ galaxy sample using the least trimmed squares algorithm (Rousseeuw & van Driessen 2006) as implemented by the *LTS_PLANEFIT* program (Cappellari et al. 2013b) to include observational errors in addition to intrinsic scatter. The plane is fit about each variable; we adopt the averages of each coefficient: $\alpha = 1.978 \pm 0.134$ and $\beta = -0.968 \pm 0.056$. We note that this is extremely close to the virial relation ($[\alpha, \beta] = [2, -1]$) and represents a significant evolution from the measured slope at $z \sim 0$, but we emphasize the potential influence of selection biases on this measurement, which often slice through the plane at nonparallel angles. However, even with this extreme evolution, the decrease in scatter about $\log R_e$ or $\log \sigma$ is minimal and comparable to the bootstrapped error estimates. Therefore, we are satisfied to adopt the $z \sim 0$ tilt for the mass fundamental plane at all redshifts; in Section 5 we include other three-parameter scaling relations.

The best-fit normalization to all galaxies in a given redshift range is shown in each panel of Figure 11 (and later of Figures 12 and 13) as a dashed black line. Normalizations to the separate star-forming and quiescent populations in each panel are included as solid blue and red lines (either for all galaxies or at fixed Sérsic index). We calculate the scatter about the fundamental plane as the standard deviation about $\log R_e$, with errors estimated by a 1000 iteration bootstrap simulation. Scatter for the total, quiescent, and star-forming populations is indicated in the lower right corner of each panel.

Figure 11(a) demonstrates clearly that to first order, star-forming and quiescent galaxies lie on nearly the same mass fundamental plane with only very small shifts in normalization ($\sim$0.06 dex). The scatter about the plane is also very similar for both star-forming (0.121 dex) and quiescent galaxies (0.107 dex). We estimate the contribution of measurement errors to this scatter by Monte Carlo simulations within the errors and find an intrinsic scatter of 0.093 dex for star-forming and 0.072 dex for quiescent galaxies.

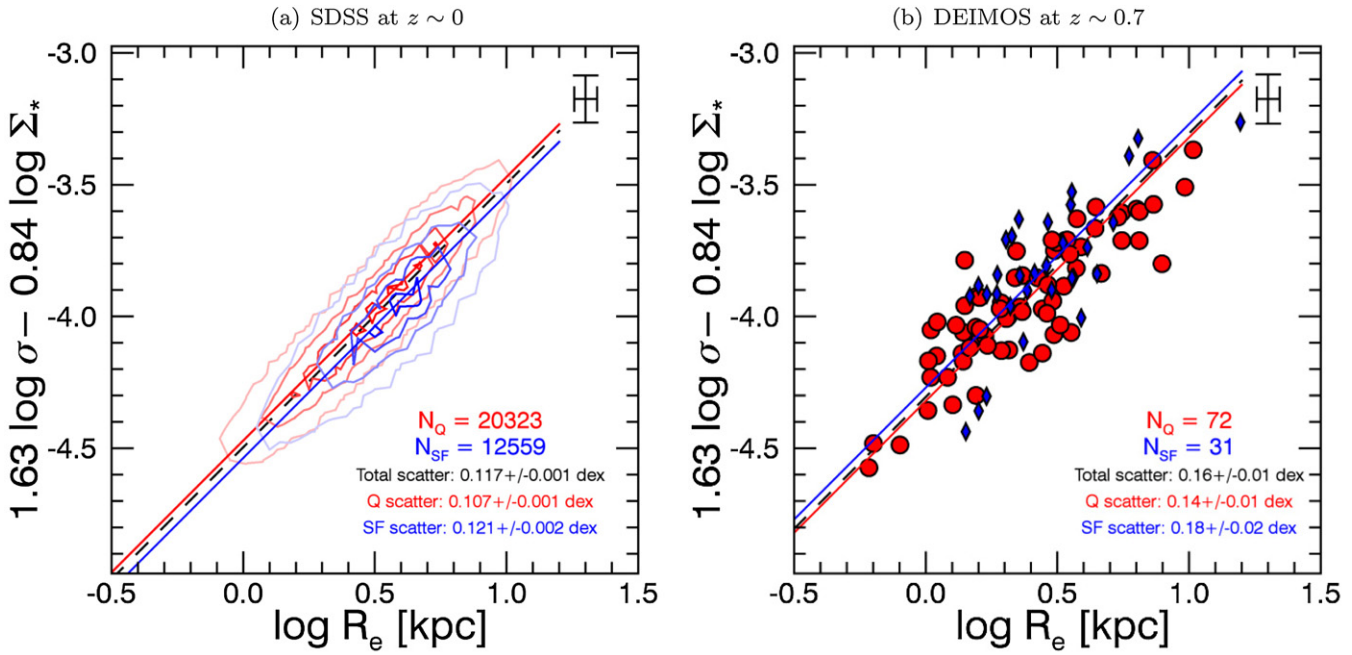

Figure 11. Mass fundamental plane, or the projected 3D surface defined by stellar mass surface density (Σ_*), velocity dispersion (σ), and circularized effective radius (R_e) of galaxies at $z \sim 0$ (panel (a)) and $z \sim 0.7$ (panel (b)). Distributions of star-forming and quiescent galaxies are given by red and blue contours, respectively (as in, e.g., Figures 5 and 8). Best-fit relations (with fixed slope and varying normalization) are included as lines in each panel. Black dashed lines indicate the best-fit normalization for all galaxies in the sample. Red (and blue) solid lines indicate the best-fit relation to all quiescent (and star-forming) galaxies. The normalization of and scatter about the mass fundamental plane for star-forming and quiescent galaxies are strikingly similar at both redshifts.

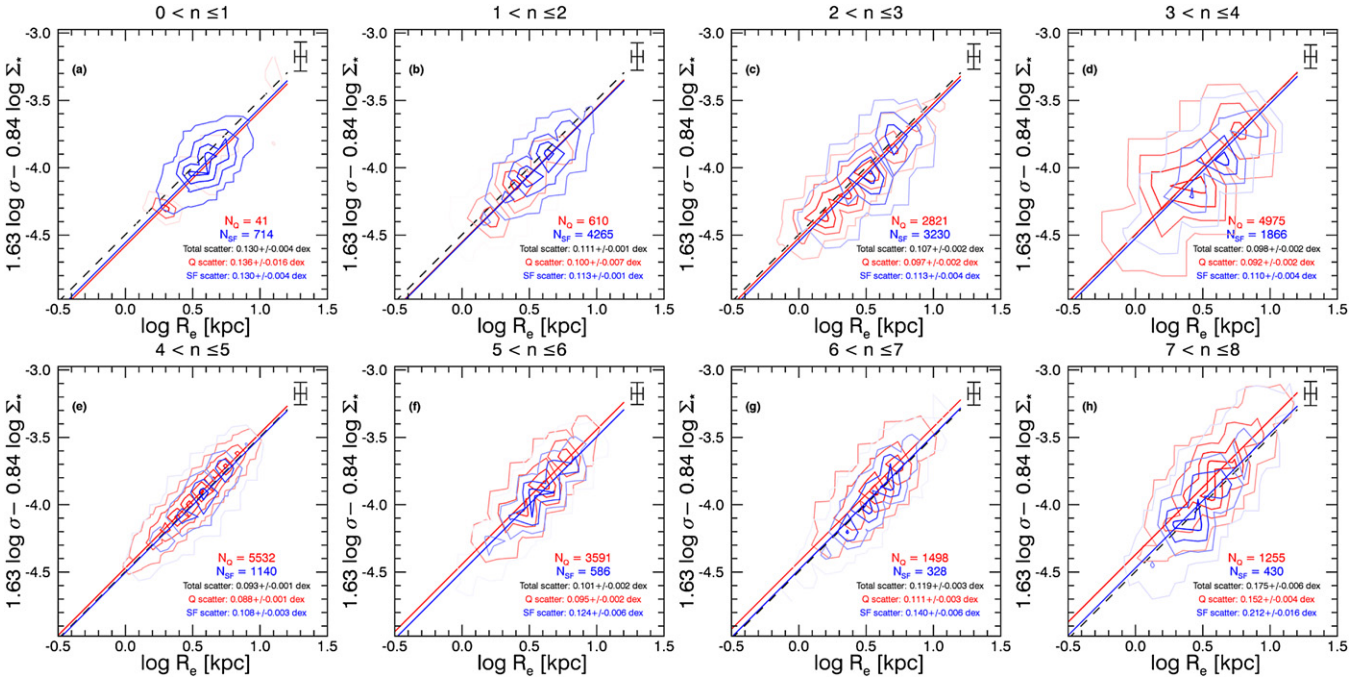

Figure 12. Mass fundamental plane for galaxies in the SDSS, now divided into bins of Sérsic index. Star-forming and quiescent galaxies are shown by red and blue dots (as in Figures 6 and 9). Best-fit relations (with fixed slope and varying normalization) are included as lines in each panel. Black dashed lines (same in all panels; see Figure 11(a)) indicate the best-fit normalization for all galaxies in the sample. Red (and blue) solid lines indicate the best-fit relation to quiescent (or star-forming) galaxies in a given Sérsic bin. The normalization of and scatter about the mass fundamental plane for star-forming and quiescent galaxies are strikingly similar. The effect of structural nonhomology is extremely subtle, with normalization varying by $\lesssim$0.1 dex as a function of Sérsic index.

At fixed Sérsic index (Figure 12), we isolate the effects of structural nonhomology on the normalization of the plane. Offsets in normalization from the overall mass fundamental plane are the largest for exponential disk-like galaxies (Figures 12(a)–(b)), in particular for quenched galaxies. For the rare sample of quiescent disk galaxies, the overall normalization is higher by ∼0.1 dex. In general, the normalization of the mass fundamental plane varies as a function of Sérsic index (and less strongly on stellar population). In this projection, low Sérsic index galaxies lie below the overall mass fundamental

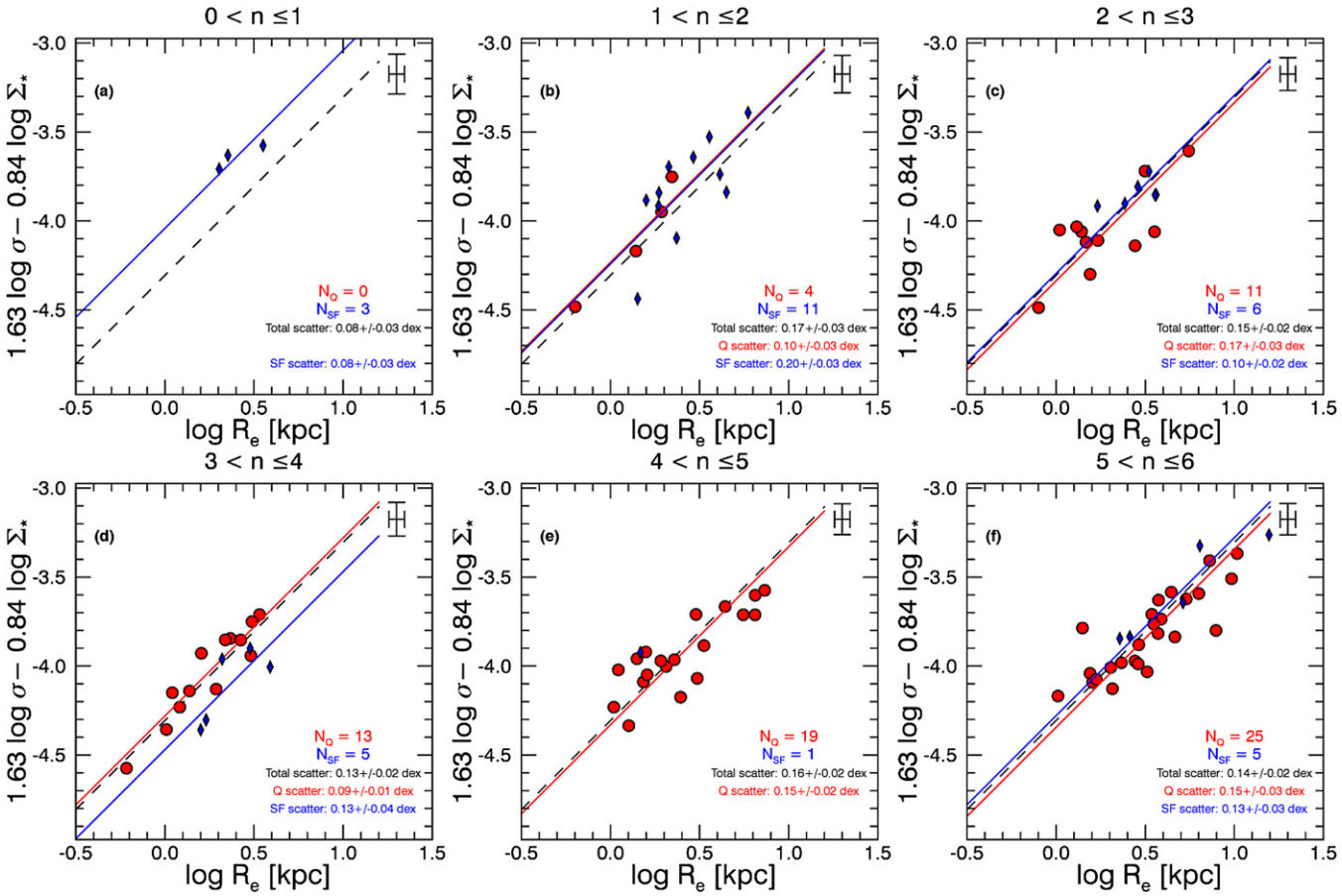

Figure 13. Mass fundamental plane for galaxies at $z \sim 0.7$. The best-fit relation to all galaxies in the sample is indicated as the dashed black line in all panels, and relations for quiescent and star-forming galaxies (altogether and in bins of Sérsic index) are shown as solid red and blue lines, respectively. Overall normalization of the mass fundamental plane differs from that in the SDSS (see Figure 12); however, it does not vary strongly with quiescence (except perhaps for the small populations of $n < 1$ or $n \sim 3$ star-forming galaxies) or Sérsic index.

plane and high Sérsic index galaxies lie above. We fit residuals from the mass fundamental plane as parameterized by

$$\Delta_{\rm MFP} = A_{\rm nh} + B_{\rm nh} n, \quad (10)$$

and we refit the scatter about the nonhomology corrected mass fundamental plane. This trend in offset with Sérsic index is the strongest for quiescent galaxies, with $[A_{\rm nh}, B_{\rm nh}] = [-0.099, 0.028]$, and including the trend decreases the scatter by 0.009 dex to 0.098. This is in contrast with the shallower relation, $[A_{\rm nh}, B_{\rm nh}] = [-0.083, 0.015]$, for star-forming galaxies, which yields only a 0.002 dex decrease in scatter to 0.119 dex. The normalization of the overall mass fundamental plane can be thought of as a population-weighted average over the structures of all galaxies; for the entire population the trend,$[A_{\rm nh}, B_{\rm nh}] = [-0.100, 0.026]$, is similar to that of the quiescent sample and an overall scatter of 0.108 dex. We emphasize that these differences are small ($\lesssim$0.1 dex) and that all galaxies lie on nearly the same plane.

At $z \sim 0.7$ the primary conclusion that star-forming and quiescent galaxies lie on roughly the same mass fundamental plane remains (Figure 11(b)). However, the details are somewhat different. First, the scatter about these relations is larger than in the SDSS sample. Partially, this is driven by the smaller sample size as reflected by larger errors in the measured scatter (estimated from bootstrap resampling). We assume that measurement errors are very similar for the two samples (e.g., errors in $M_\star/L$), implying intrinsic scatter of $\sim$0.14 dex for all galaxies and $\sim$0.12 dex for quiescent galaxies. This suggests that measurement errors have been underestimated for this sample or that the tightness of the mass fundamental plane decreases with redshift. Measured scatter about the mass fundamental plane is slightly larger for star-forming galaxies, but this is within the errors. Additionally, the overall normalization is slightly higher than at $z \sim 0$ ($\sim$0.2 dex), as shown in Bezanson et al. (2013). We discuss possible explanations for this effect in Section 6. Furthermore, while there are slight offsets from the mass fundamental plane at fixed Sérsic index (Figure 13), these are partially driven by small sample size. We conclude that this sample is insufficient to definitively assess the effects of structural nonhomology on the mass fundamental plane at $z > 0$.

Table 3
Mass Faber–Jackson Parameters

Sample	$A_{\rm FJ}$	$B_{\rm FJ}$	$A_{\rm FJ}^{\rm Q}$	$B_{\rm FJ}^{\rm Q}$	$A_{\rm FJ}^{\rm SF}$	$B_{\rm FJ}^{\rm SF}$
SDSS	0.41 ± 0.00	-2.25 ± 0.02	0.37 ± 0.00	-1.80 ± 0.02	0.39 ± 0.00	-2.06 ± 0.03
DEIMOS	0.34 ± 0.04	-1.37 ± 0.43	0.28 ± 0.06	-0.68 ± 0.62	0.46 ± 0.11	-2.60 ± 1.11

Note. Best-fit mass Faber–Jackson relations at $z \sim 0$ and $z \sim 0.7$ (see Equation (11)).

Table 4
Measured and Intrinsic Scatter in Velocity Dispersions Inferred from Scaling Relations

Relation	rms	Intrinsic rms	rms (Q)	Intrinsic rms (Q)	rms (SF)	Intrinsic rms (SF)
SDSS: $z \sim 0$						
Faber–Jackson	0.112 ± 0.000	0.101	0.105 ± 0.001	0.095	0.107 ± 0.001	0.094
Mass fundamental plane	0.072 ± 0.001	0.055	0.066 ± 0.001	0.049	0.075 ± 0.001	0.057
Virial theorem ($k_V = 5$)	0.074 ± 0.001	0.064	0.070 ± 0.001	0.061	0.075 ± 0.001	0.063
Virial theorem ($k_V(n)$)	0.069 ± 0.001	0.058	0.063 ± 0.001	0.053	0.078 ± 0.001	0.066
DEIMOS: $z \sim 0.7$						
Faber–Jackson	0.14 ± 0.01	0.13	0.14 ± 0.01	0.13	0.13 ± 0.02	0.12
Mass fundamental plane	0.10 ± 0.01	0.08	0.09 ± 0.01	0.07	0.11 ± 0.01	0.10
Virial theorem ($k_V = 5$)	0.09 ± 0.01	0.08	0.08 ± 0.01	0.07	0.11 ± 0.01	0.10
Virial theorem ($k_V(n)$)	0.10 ± 0.01	0.09	0.08 ± 0.01	0.07	0.12 ± 0.01	0.11

Notes. Measured and intrinsic scatter in velocity dispersion from various scaling relations at $z \sim 0.7$, for all galaxies and then separately for quiescent (Q) and star-forming (SF) galaxies. Inferred velocity dispersions are calculated using the following equations: Faber–Jackson from Equation (11), mass fundamental plane from Equation (12), and virial theorem with constant from Equation (14) and with Sérsic-dependent constant from Equation (15).

5. SCATTER AND THE FORM OF THE 3D MASS PLANE

Despite the structural and dynamical differences between the populations of star-forming and quiescent galaxies, we have shown that all galaxies follow roughly the same 3D relationship among velocity dispersion, size, and stellar mass or stellar mass surface density. In this section we investigate whether the mass fundamental plane defined in Section 4 is the optimal form of the 3D surface. Here we consider four scaling relations: the mass Faber–Jackson relation, the mass fundamental plane, the virial plane, and a virial relation with a Sérsic-dependent constant. Measured relations are included in Tables 2 and 3. Specifically, we assess the ability of a given relation to predict the velocity dispersion of a galaxy, as measured by the scatter between the inferred and measured dispersions. Measured and intrinsic scatter for each relation is reported in Table 4.

Figure 14 shows these comparisons for galaxies in the SDSS sample. Figure 14(a) shows the velocity dispersion predicted from the mass Faber–Jackson relation (shown in Figure 8(a)):

$$\log \sigma_{\rm inf,FJ} = {\rm A_{FJ}} \log\ M_\star + {\rm B_{FJ}}, \quad (11)$$

versus measured velocity dispersion (large panel), residuals as a function of velocity dispersion (lower panel), and a histogram of residuals for star-forming and quiescent galaxies (right) separately. This and the following relations assume that velocity dispersions are measured in $\rm km\,s^{-1}$, sizes are measured in kpc, and stellar masses are quoted in $M_\odot$. The mean and standard deviations of the residuals for star-forming and quiescent galaxies are indicated as blue/red dots with error bars to the right of the histograms. Scatter for all galaxies and quiescent/star-forming populations is given in black, red, and blue text in the upper left corner.

The scatter in this relation is highest of the four tested scaling relations, with a scatter in velocity dispersion of ∼0.11 dex for all populations. Furthermore, the residuals exhibit additional correlations in the bottom panel, with offset median values for star-forming and quiescent galaxies. We note that separately measuring the mass Faber–Jackson relation for star-forming and quiescent galaxies reduces the scatter only minimally (by 0.01 dex), although it does remove residual correlations (see Appendix B).

Figure 14(b) has the same layout as Figure 14(a) but compares the velocity dispersion predicted by the mass fundamental plane:

$$\log \sigma_{\rm inf,massFP} = (\log R_e - \beta \log \Sigma_\star - \gamma)/\alpha, \quad (12)$$

to the measured velocity dispersion (measured normalizations γ are provided in Table 2). The scatter about this relation is lower (0.07 dex), though there seems to be a slight residual trend, possibly indicating a slight tilt relative to the Hyde & Bernardi (2009) mass fundamental plane.

Another possible relation to connect the dynamical and structural properties of galaxies is the virial theorem, which states that

$$M_\star = \frac{M_\star}{M_{\rm dyn}} \frac{k R_e \sigma^2}{G}. \quad (13)$$

The constant in this equation, k, can be estimated from analytical models or measured empirically. Based on the observed dynamical and structural properties of local elliptical galaxies, $k \approx 5$ (Cappellari et al. 2006). Figure 14(c) compares measured dispersion to the velocity dispersion predicted by the virial theorem:

$$\log \sigma_{\rm inf,V} = 0.5\,(\log M_\star - \log R_e) + C_V, \quad (14)$$

in which the constant is a combination of the gravitational constant, G, the virial constant, and a normalization as $C_V = 0.5 \log((G/(M_\star/M_{\rm dyn})(5)))$. See Appendix D for a discussion of the relationship between dynamical and stellar mass. We fit the normalization and find $C_V = 2.848$ at $z \sim 0$, $C_V = -2.956$ at $z \sim 0.7$. This relation yields a similar overall scatter to the mass fundamental plane (0.07 dex), although this is slightly higher for star-forming galaxies (0.08 dex).

Dynamical models of galaxies with varied stellar distributions predict a variation of the virial constant, for example, with Sérsic index (e.g., Ciotti 1991; Bertin et al. 2002; Cappellari et al. 2006). Given the range in galaxy morphology probed by this study, this could be important. Figure 14(d) compares measured with inferred velocity dispersion calculated with the virial theorem, but including an analytically derived virial constant that depends on Sérsic index:

$$\log \sigma_{\rm inf,V}(n) = 0.5\,(\log M_\star - \log R_e) + C_{V(n)}, \quad (15)$$

in which the constant $C_{V(n)} = 0.5 \log((G/M_\star/M_{\rm dyn})) - 0.5 \log k_V(n)$. The Sérsic-dependent constant, $k_V(n) \approx 8.87 - 0.831n + 0.0241n^2$ (Cappellari et al. 2006), is derived analytically by solving the spherically symmetric Jeans equation

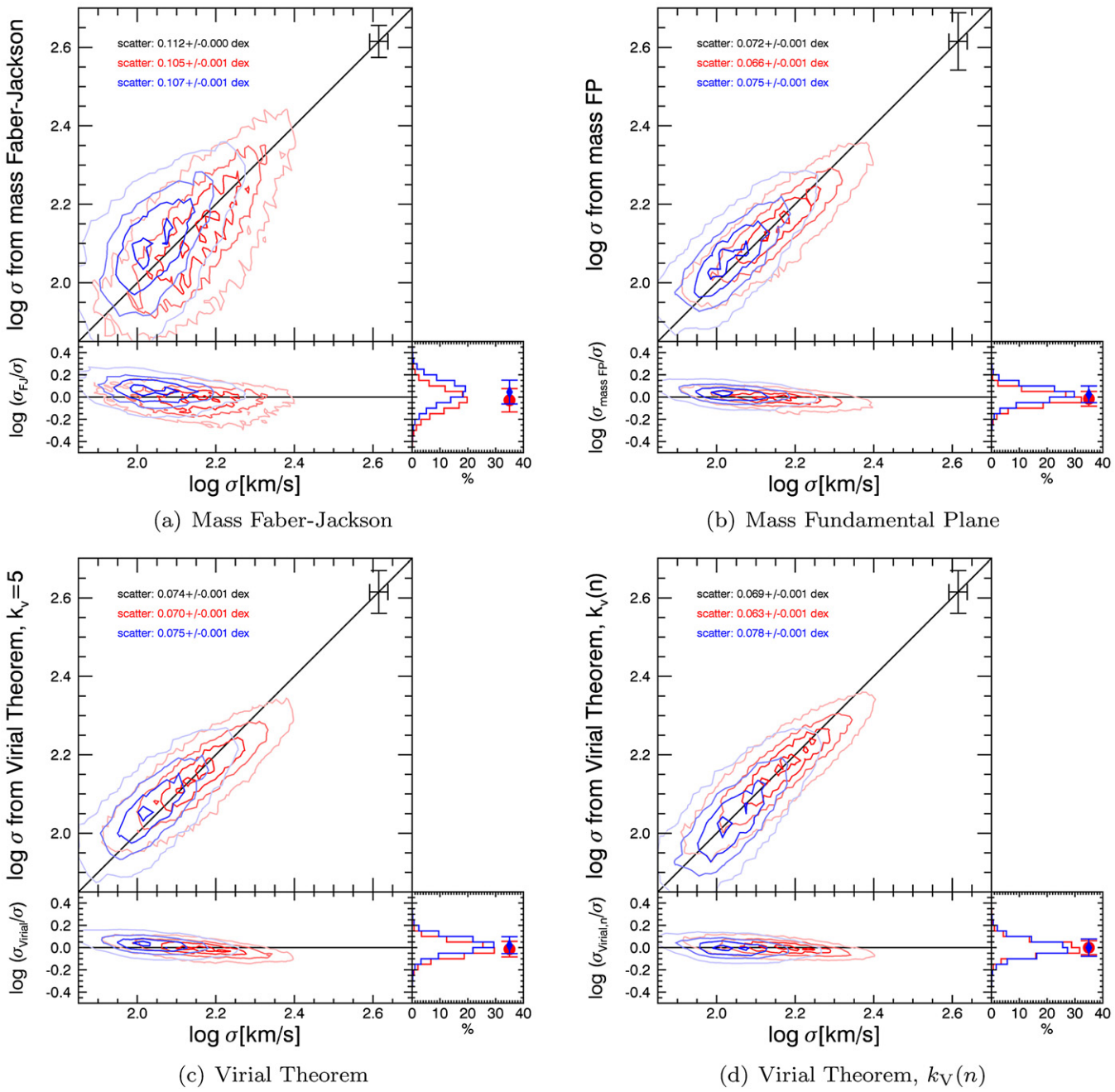

Figure 14. Comparison of the tightness of scaling relations in the SDSS as revealed by predicted velocity dispersion vs. measured velocity dispersion (square panels) and residuals from those relations (bottom panels). (a) Velocity dispersion predicted by the mass Faber–Jackson relation (see also Figure 18) vs. measured velocity dispersion. (b) Velocity dispersion predicted by the mass fundamental plane vs. measured velocity dispersion. (c) Velocity dispersion predicted by the virial theorem with a single constant (independent of nonhomology) vs. measured velocity dispersion. (d) Velocity dispersion predicted by the virial theorem with a Sérsic-dependent constant vs. measured velocity dispersion. In each case, including galaxy sizes (as in panels (b)–(d)) decreases the scatter in the scaling relations for quiescent and star-forming galaxies alike. However, the scatter is comparable about both virial planes and the mass fundamental plane.

with the assumption that mass follows a Sérsic profile and all orbits are isotropic. We allow the normalization to vary to account for differences in $(M_\star/M_{\rm dyn})$, finding $C_{V(n)}(z \sim 0) = -2.539–0.5 \log k_V(n)$ and $C_{V(n)}(z \sim 0.7) = -2.646–0.5 \log k_V(n)$. Again the overall scatter is the same (0.07 dex), which is an average between a tightened fit for quiescent galaxies (0.06 dex) and an increase in scatter for star-forming galaxies (0.08 dex).

The overall scatter in the latter three relations is comparable: ∼0.07 dex for the full galaxy population in each case, indicating the importance of including size measurements in these scaling relations. Although the scatter for the quiescent galaxy population decreases slightly when a Sérsic-dependent virial constant is included (∼0.06 dex), and trends in the residuals differ only subtly, all three surfaces adequately describe the relationship between galaxy structures and dynamics for star-forming and quiescent galaxies. This is not the case for scatter about $\log R_e$ (see Appendix C), in which the mass fundamental plane exhibits much lower scatter; however, this may be driven by correlated measurement errors.

Figure 15 demonstrates that similar results hold at $z \sim 0.7$. Again the scatter derived from the mass Faber–Jackson is

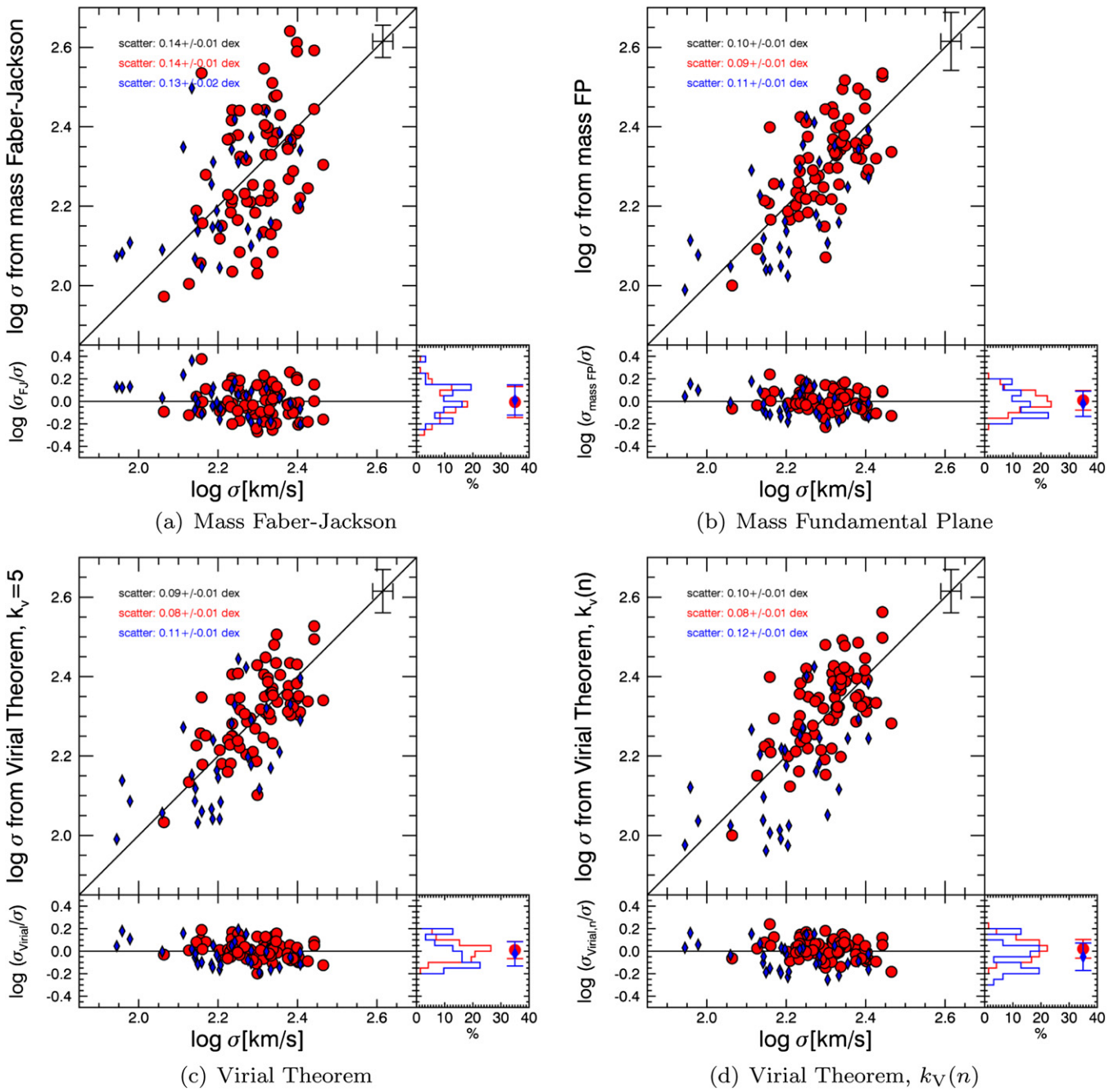

Figure 15. Comparison of the tightness of scaling relations (layout as in Figure 14) at $z \sim 0$. Velocity dispersion predicted by (a) the mass Faber–Jackson, (b) the mass fundamental plane, (c) the virial theorem with a single constant, and (d) the virial theorem with a Sérsic-dependent constant vs. measured velocity dispersion. As at $z \sim 0$, including galaxy size decreases the scatter in galaxy scaling relations, with very subtle differences between the three possible 3D surfaces.

larger (Figure 15(a)) than for the mass fundamental plane (Figure 15(b)) or the virial theorem, both without (Figure 15(c)) and with (Figure 15(d)) a Sérsic-dependent constant. The overall scatter in the three latter relations is roughly the same, although it is larger for star-forming galaxies, in contrast with the $z \sim 0$ SDSS sample.

6. DISCUSSION AND CONCLUSIONS

We have shown that despite the structural and dynamical differences between star-forming and quiescent galaxies, all massive ($\sigma \gtrsim 100\,\mathrm{km\,s^{-1}}$) galaxies lie within the same 3D phase space when structures (size and profile shape) and stellar dynamics (velocity dispersion) are included concurrently. The data do not suggest a significant preference for any of the specific 3D surfaces examined in this work: the mass fundamental plane, the virial plane, or the space defined by the virial theorem with a Sérsic-dependent constant.

Cappellari et al. (2013a) pointed out that the existence of a mass fundamental plane (or "mass plane") for elliptical galaxies does not strongly constrain galaxy formation models; it is simply a statement that galaxies are in virial equilibrium. However, in the context of this work, the fact that star-forming and quiescent galaxies both lie on mass fundamental planes and that the normalization is so similar could have important implications for galaxy formation models.

The inclusion of star-forming and quiescent galaxies in the same scaling relations can provide interesting constraints on

galaxy formation models and can be useful for observational astronomy at high redshifts; however, it is not a new technique. Taylor et al. (2010) demonstrated that the stellar masses of galaxies of all types were directly correlated with dynamical masses derived from sizes, velocity dispersions, and Sérsic indices, using comparable galaxies from the SDSS. This work is also similar to studies of the fundamental manifold (e.g., Zaritsky et al. 2006, 2008, 2011). In particular, Zaritsky et al. (2008) demonstrated that both disks and spheroids across a wide range of masses lie on the same plane in velocity, size, and surface brightness space when allowing for variation in mass-to-light ratios. In that work, the velocity (V) was composed of either rotational velocity or intrinsic velocity dispersion; by measuring the line-of-sight, projected velocity dispersion as in this work, σ is nearly the same quantity as $V^2 \equiv 0.5V_r^2 + \sigma^2$ in the fundamental manifold formalism. In this paper we verify the existence of a similar mass fundamental plane in which mass-to-light ratios are derived from stellar population synthesis modeling alone. Furthermore, we extend these conclusions to higher redshift and propose that such unified scaling relations are not just an interesting property of galaxies, but an important and flexible tool to study galaxies through cosmic time.

Although this study shows that quenched and star-forming galaxies exist within the same 3D space, they still populate different regions of that space. Therefore, the processes that are responsible for driving the transition or quenching of galaxies from one population may alter galaxy structures and dynamics and must do so within the allowed space defined by the mass fundamental plane. It has been suggested that star-forming galaxies at high redshift are structurally similar to local elliptical galaxies, even though they are larger at a fixed epoch (e.g., Franx et al. 2008; van der Wel et al. 2014). The evolution of galaxies in this plane is certainly due to a combination of such simple, passive evolution and stronger structural evolution, likely driven by galaxy merging. Another potentially important constraint is the weak dependence of the structural and dynamical scaling relations on profile shape, as quantified by Sérsic index. The shape of the mass fundamental plane and the projections explored in this paper, the mass–size and Faber–Jackson relations, vary subtly with Sérsic n. Therefore, models of passive evolution must also compare detailed structures, not just sizes, of galaxy populations at different redshifts. With a larger sample of galaxy dynamics across galaxy populations and time, one could compare the structures, both sizes and profile shapes, and dynamics of high-redshift disk galaxies with those of quenched descendent galaxies at later times and assess the relative importance of various physical processes.

To first order the mass fundamental plane for quiescent galaxies does not evolve strongly since $z \sim 2$ (Bezanson et al. 2013); however, the normalization of the plane is slightly different between the two epochs probed by this study ($\sim$0.2 dex). This could be due to a combination of observational and/or physical reasons. First, dynamics of galaxies are observed within somewhat different spectroscopic apertures. Although aperture corrections are made based on empirical velocity dispersion profiles and the corrections themselves are generally small ($\sim$4% in the SDSS and $\sim$2% at $z \sim 0.7$), these relations are found for local ellipticals and could vary with redshift or morphological type. Furthermore, $M_\star/L$ are measured within different physical apertures between the two redshift slices, and color gradients could introduce offsets in the measured mass fundamental plane. Additionally, it could be related to the distribution of Sérsic indices of the two samples: the $z \sim 0.7$ sample of galaxies has a larger fraction of galaxies with high Sérsic indices $n > 4$. In the SDSS we showed that the normalization of the mass fundamental plane varies subtly with Sérsic index relative to the population-weighted average (Figure 12), bringing high-n galaxies closer to the normalization of the $z \sim 0.7$ mass fundamental plane.

Perhaps the more physically interesting case would involve slight evolution in the density profiles in the central regions of galaxies: either in stars or in dark matter. As galaxies grow through cosmic time, the more massive ones appear to be growing in an "inside-out" manner (e.g., Bezanson et al. 2009; Hopkins et al. 2009a). This translates to an increase in Sérsic indices (e.g., van Dokkum et al. 2010; Patel et al. 2013) with time for massive galaxies. In Figures 12 and 13 we demonstrated the slight dependence of the mass fundamental plane normalization on structure (quantified by Sérsic index). Different distributions of stellar density profile shapes imply slightly different dynamics.

Additionally, this could be due to a variation in the dark matter fraction in the inner regions of galaxies. Indications of evolution in $M_{\rm DM}/M_\star(<R_e)$ with redshift have been suggested theoretically (Hopkins et al. 2009b), based on simulations (Hilz et al. 2013), and empirically (e.g., van de Sande et al. 2013) as the stellar components undergo significant growth with time. Only with a clear understanding of the relative growth of dark matter and stellar components and the shape of the combined gravitational potential could we assess the resulting impact on the evolution of the normalization of the mass fundamental plane.

Potentially the most interesting implication of this work in the context of observational studies of galaxies at high redshift is that it suggests that given the measured stellar mass and size of a galaxy, regardless of its light profile shape, whether it is a disk or spheroidal, and whether it is forming stars or not, we can predict its stellar dynamics. These dynamics can be used to create a census of galaxies through cosmic time as a function of their velocity dispersions (see, e.g., Bezanson et al. 2011, 2012). Flexibility with respect to galaxy morphology is particularly important in the context of building evidence that massive galaxies were more *disklike*, based on axis ratio distributions (e.g., van der Wel et al. 2011; Weinzirl et al. 2011; Bruce et al. 2012; Chevance et al. 2012; Chang et al. 2013) and Sérsic indices (e.g., van Dokkum et al. 2010; Patel et al. 2013).

Furthermore, when following populations of galaxies through cosmic time, dynamics are likely to be the most stable property of individual galaxies with time (see, e.g., Bezanson et al. 2011, 2012; Belli et al. 2014a, 2014b). Under this assumption, the ability to infer the dynamics of a galaxy from less observationally expensive data is invaluable. As an example, there is a growing body of literature following the detection and verification of compact quiescent galaxies at $z \gtrsim 1.5$ (e.g., Daddi et al. 2005; Trujillo et al. 2006; van Dokkum et al. 2008; Szomoru et al. 2010; van de Sande et al. 2013) and discussion of possible formation mechanisms, particularly the identification of star-forming progenitors (e.g., Barro et al. 2013, 2014a; Patel et al. 2013; Toft et al. 2014). Therefore, the best way to connect progenitors and these descendants may be by their dynamics. Ideally, dynamics would be directly measured using deep spectroscopy; however, this is extremely challenging even in optimal cases. At $z \gtrsim 2$, stellar absorption line kinematics have only been measured directly for roughly a dozen quiescent galaxies (e.g., van Dokkum et al. 2009; van de Sande et al.

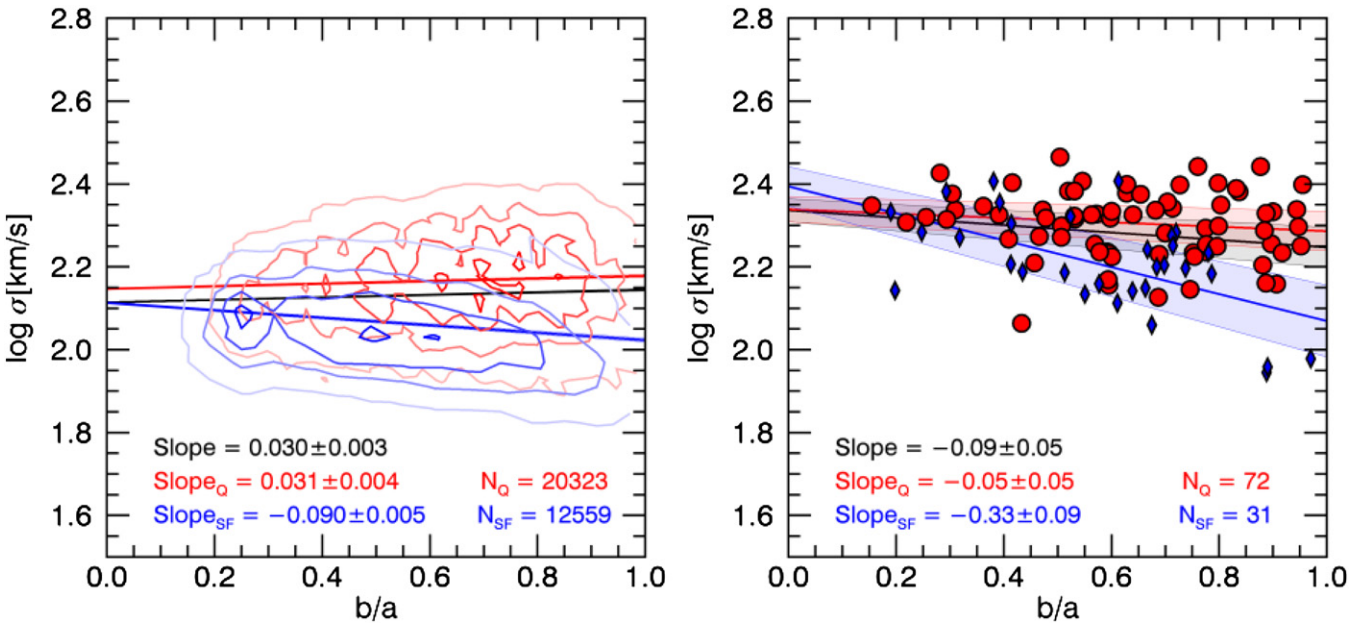

Figure 16. Velocity dispersion vs. axis ratio (b/a) for galaxies in the SDSS (left panel) and at $z \sim 0$ (right panel). In the left panel, the distributions of quiescent galaxies and star-forming galaxies are indicated by red and blue contours, respectively; in the right panel, by red and blue dots. Linear fits are included as black (all galaxies), red (quiescent galaxies), and blue (star-forming galaxies) solid lines. Quiescent galaxies do not exhibit trends as a function of projected axis ratio, while rounder (higher b/a) galaxies have slightly lower measured velocity dispersions at both redshifts. This trend is slightly stronger at $z \sim 0.7$ (right). These data suggest that inclination contributes subtly to the scatter in scaling relations of star-forming galaxies.

2011; Onodera et al. 2012; van de Sande et al. 2013; Toft et al. 2012; Belli et al. 2014b) and only indirectly from gas dynamics for star-forming or submillimeter galaxies (e.g., Tacconi et al. 2008; Toft et al. 2014; Barro et al. 2014b; Nelson et al. 2014). If the existence of a common mass fundamental plane extends to these early times, it implies that we can efficiently connect star-forming and quenched galaxies using inferred dynamics with relative ease from excellent, and existing, *HST* data from the CANDELS (Grogin et al. 2011; Koekemoer et al. 2011) and 3DHST (Brammer et al. 2012; Skelton et al. 2014) surveys.

Finally, star-forming and quenched galaxies lie on a common mass fundamental plane in both of the samples presented in this work; however, only the SDSS sample is large enough to probe the relations as a function of morphology. Although there are hints that nonhomology affects the normalization of the mass fundamental plane differently as a function of redshift, only with a much larger sample of galaxies, including a full range of star-forming and quiescent disks and spheroidals, could we begin to assess this evolution and evaluate the importance of such subtle effects as morphological and baryonic to dark matter profile evolution through cosmic time.

The authors wish to acknowledge the funding agencies, institutional support, and observatories that supported the collection and analysis of the data included in this work, without which this project would not have been possible. We also wish to thank Rik Williams and Ryan Quadri for providing access to the most recent UDS photometric catalog. Finally, we thank the anonymous referee whose feedback contributed to the quality of the final version of this article.

Support for this work was provided by NASA through Hubble Fellowship grant #HF-51318.01-A awarded by the Space Telescope Science Institute, which is operated by the Association of Universities for Research in Astronomy, Inc., for NASA, under contract NAS 5-26555.

Some of the data presented herein were obtained at the W. M. Keck Observatory, which is operated as a scientific partnership among the California Institute of Technology, the University of California, and the National Aeronautics and Space Administration. The Observatory was made possible by the generous financial support of the W. M. Keck Foundation. The authors wish to recognize and acknowledge the very significant cultural role and reverence that the summit of Mauna Kea has always had within the indigenous Hawaiian community. We are most fortunate to have the opportunity to conduct observations from this mountain. The analysis pipeline used to reduce the DEIMOS data was developed at UC Berkeley with support from NSF grant AST-0071048.

Funding for the SDSS and SDSS-II has been provided by the Alfred P. Sloan Foundation, the Participating Institutions, the National Science Foundation, the U.S. Department of Energy, the National Aeronautics and Space Administration, the Japanese Monbukagakusho, the Max Planck Society, and the Higher Education Funding Council for England. The SDSS Web site is http://www.sdss.org/. The SDSS is managed by the Astrophysical Research Consortium for the Participating Institutions. The Participating Institutions are the American Museum of Natural History, Astrophysical Institute Potsdam, University of Basel, University of Cambridge, Case Western Reserve University, University of Chicago, Drexel University, Fermilab, the Institute for Advanced Study, the Japan Participation Group, Johns Hopkins University, the Joint Institute for Nuclear Astrophysics, the Kavli Institute for Particle Astrophysics and Cosmology, the Korean Scientist Group, the Chinese Academy of Sciences (LAMOST), Los Alamos National Laboratory, the Max-Planck-Institute for Astronomy (MPIA), the Max-Planck-Institute for Astrophysics (MPA), New Mexico State University, Ohio State University, University of Pittsburgh, University of Portsmouth, Princeton University, the United States Naval Observatory, and the University of Washington.

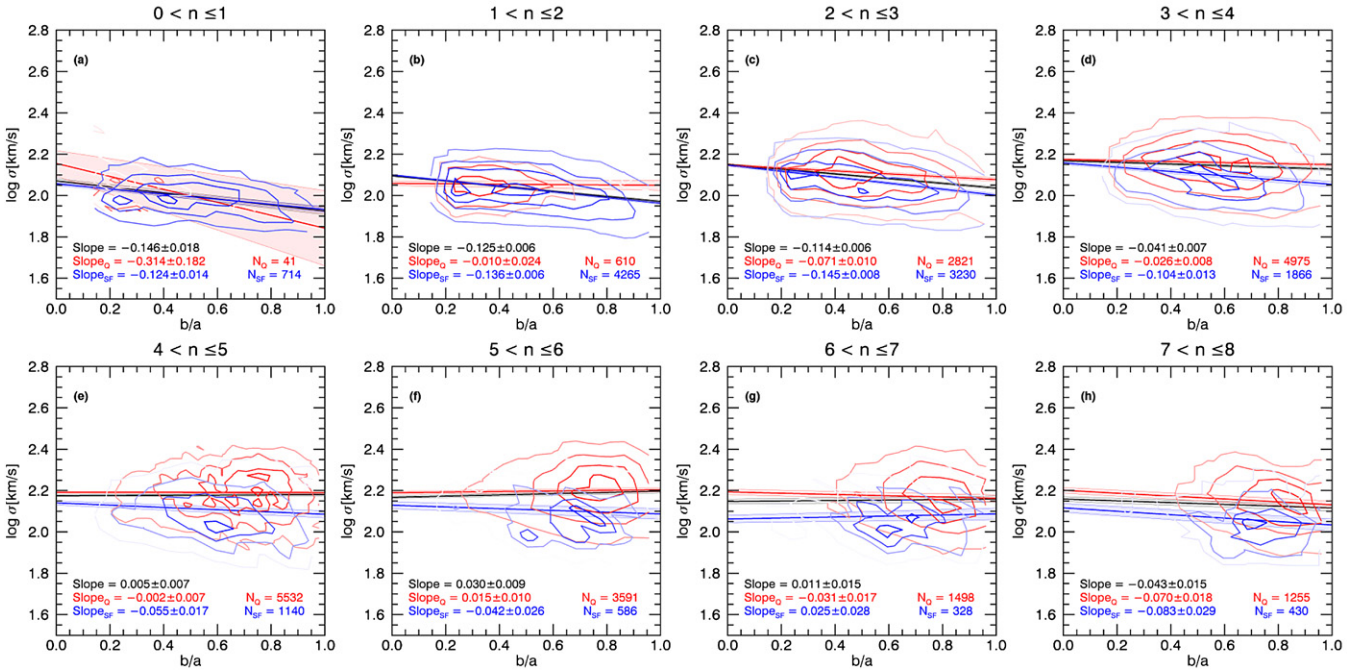

Figure 17. Velocity dispersion vs. axis ratio (b/a) for galaxies in the SDSS, separated by best-fit Sérsic index. Annotations and symbols are as in Figure 16. For galaxies in the SDSS, it is apparent that the weak trends in velocity dispersion with axis ratio are important only for galaxies that more disklike ($n \lesssim 4$), particularly for those that are star-forming.

This work is based partially on observations taken by the 3D-HST Treasury Program (GO 12177 and 12328) with the NASA/ESA *HST*, which is operated by the Association of Universities for Research in Astronomy, Inc., under NASA contract NAS5-26555.

APPENDIX A

THE EFFECTS OF INCLINATION ON MEASURED VELOCITY DISPERSION

In Section 2.6 we suggested a dependence of the measured velocity dispersion of a disk galaxy on observed inclination (Equation (8)). Based on this empirical relation, measured velocity dispersion will be a combination of intrinsic dispersion and inclination-corrected rotational velocity. However, increasing intrinsic velocity dispersion, potentially due to the presence of a significant bulge component, would minimize the importance of inclination on the measured velocity dispersions. Although the inclination of a galaxy cannot be directly measured from the available data, we can use the projected axis ratio as a proxy measurement. In the following figures, we assess trends in measured velocity dispersion as a function of axis ratio, and therefore inclination, for the entire population of galaxies and separated by stellar populations and morphologies.

Figure 16 shows trends in measured velocity dispersion as a function of axis ratio for galaxies in the SDSS (left panel) and at $z \sim 0.7$ (right panel). As in the previous figures, quiescent galaxies are indicated by red contours (SDSS) or circles ($z \sim 0.7$); star-forming galaxies are indicated by blue contours or symbols. Linear fits to the full population (black), quiescent (red), and star-forming (blue) galaxies are included as solid lines. Errors in the linear fits are estimated via bootstrap resampling of each sample, and the 1σ range of the fits is indicated by the shaded regions. Slopes of the lines are indicated in the lower left corner of each panel. At both redshifts, there is little to no statistically significant trend in velocity dispersion with projected axis ratio for quiescent galaxies. However, there is a weak trend at each redshift for star-forming galaxies such that velocity dispersion decreases slightly for rounder galaxies. This effect is small, suggesting that although inclination does impact measured velocity dispersions, it is a very weak effect. In the SDSS, the mean change in velocity dispersion across the full range in axis ratio (from $b/a \sim 0.2$ to $b/a \sim 1$) implies a discrepancy of only 0.07 dex or a factor of 1.18 in velocity dispersion. This effect appears to be stronger at $z \sim 0.7$, at which the same change in b/a would imply $\sim$0.26 dex difference or a factor of $\sim$1.8 in velocity dispersion. However, we note that the potential incompleteness of this sample for rounder galaxies may impact the measurement of this trend. Furthermore, the method of measuring galaxy dynamics differs subtly between the two samples: in the SDSS, the velocity dispersion is measured within the 3″ fiber, whereas the $z \sim 0.7$ spectra are integrated across a 1″ slit. At $z \sim 0.06$, 3″ corresponds to a physical scale of $\sim$3.5 kpc, compared to $\sim$7 kpc of the 1″ slit at $z \sim 0.7$. Additionally, given the size evolution of galaxies, this larger physical aperture corresponds to an even larger fraction of the galaxies that are being probed in the higher-redshift sample. This suggests that within the centers of galaxies, such as those probed by the SDSS fibers, the dynamics are more dominated by central bulges. However, at higher redshift, when the dynamics are probed in larger apertures, the effects of inclination will be stronger and could contribute to the scatter in such dynamical scaling relations.

In Figure 17 we evaluate the dependence of this trend on structural parameters (in the SDSS only), splitting galaxies into bins of Sérsic index. Color-coding, notations, and symbols are as in Figure 16. In these panels, we see that the trends with axis ratio are stronger for more disk-like galaxies (at lower Sérsic n), for both star-forming and quiescent galaxies. Above $n \sim 4$, the trends all but disappear. This is partially due to the fact that these disky galaxies likely have more oblate structures, and therefore axis ratio will be a more sensitive probe of

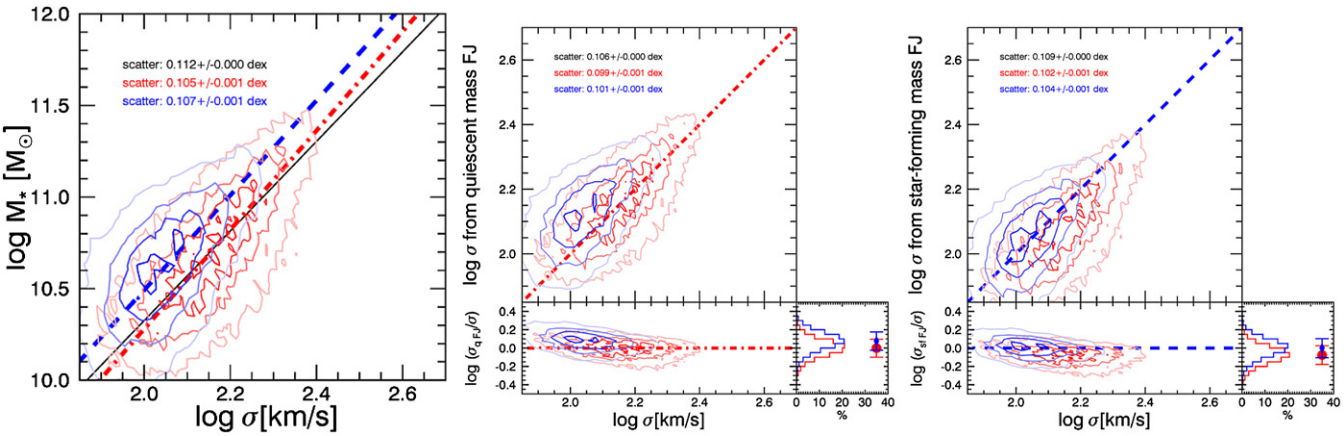

Figure 18. Mass Faber–Jackson relation (left panel) in the SDSS. The best-fit relation is measured for all galaxies (solid black line) but differs slightly in slope and normalization for star-forming (dashed blue line) and quiescent (dot dashed red line) galaxies. Expanding on Figure 14, we demonstrate that the scatter in the velocity dispersion predicted by the mass Faber–Jackson relation vs. measured velocity dispersion does not decrease by adopting the best-fit relation to star-forming (middle panel) or quiescent (right panel) galaxies.

Table 5
Measured and Intrinsic Scatter in log R_e from Scaling Relations

Relation	rms	$\mathrm{rms_{int}}$	rms (Q)	$\mathrm{rms_{int}}$ (Q)	rms (SF)	$\mathrm{rms_{int}}$ (SF)
SDSS: $z \sim 0$						
Mass fundamental plane $\log R_e = 1.63 \log \sigma - 0.84 \log \Sigma_\star + 4.496$	0.117 ± 0.001	0.088	0.107 ± 0.001	0.074	0.121 ± 0.002	0.094
Virial theorem ($k_V = 5$) $\log R_e = \log M_\star - 2.0 \log \sigma - 5.695$	0.149 ± 0.001	0.130	0.140 ± 0.001	0.121	0.150 ± 0.002	0.132
Virial theorem ($k_V(n)$) $\log R_e = \log M_\star - 2.0 \log \sigma + \log k_V(n) - 5.078$	0.139 ± 0.001	0.118	0.127 ± 0.001	0.104	0.156 ± 0.002	0.138
DEIMOS: $z \sim 0.7$						
Mass fundamental plane $\log R_e = 1.63 \log \sigma - 0.84 \log \Sigma_\star + 4.306$	0.16 ± 0.01	0.13	0.14 ± 0.01	0.12	0.18 ± 0.02	0.16
Virial theorem ($k_V = 5$) $\log R_e = \log M_\star - 2.0 \log \sigma - 5.911$	0.18 ± 0.01	0.16	0.15 ± 0.01	0.13	0.22 ± 0.02	0.20
Virial theorem ($k_V(n)$) $\log R_e = \log M_\star - 2.0 \log \sigma + \log k_V(n) - 5.292$	0.20 ± 0.01	0.19	0.17 ± 0.01	0.15	0.24 ± 0.02	0.23

Notes. Measured and intrinsic scatter in log R_e from various scaling relations, for all galaxies and then separately for quiescent (Q) and star-forming (SF) galaxies. Quantitative relations are included in the table, and the Sérsic-dependent virial constant from (Cappellari et al. 2006) is approximated by $k_V(n) = 8.87–0.831n + 0.0241n^2$) as in Equation (15).

inclination. Additionally, one would expect these galaxies to have more rotational support (higher v/σ), which determines the contribution of inclination to Equation (8). Although this paper demonstrates that the scaling relations of massive galaxies can be determined without the inclusion of an inclination correction, we conclude that the inclination of galaxies with disklike morphologies will contribute a small amount of scatter to the relations. This may become increasingly important for higher-redshift studies, as the effect will likely increase with the physical scale of the spectroscopic aperture relative to the decreasing sizes of evolving galaxy populations.

APPENDIX B

DOES THE MASS FABER–JACKSON RELATION TIGHTEN FOR SEPARATE GALAXY POPULATIONS?

The stellar mass Faber–Jackson relation for star-forming and quiescent galaxies differs in normalization and slope; therefore, the measured relation for the overall population of galaxies at a given redshift will be an average of the two relations. In Section 5 we demonstrated that the scatter about the Faber–Jackson relation is greater than the scatter in relations that incorporate galaxy sizes. Locally, the fundamental plane for elliptical galaxies exhibits less scatter than its projection, the Faber–Jackson relation; however, in this appendix we investigate whether some of this scatter is due to adopting a uniform definition of the Faber–Jackson relation for both galaxy populations.

Figure 18(a) shows the Faber–Jackson relation for galaxies in the SDSS. The black line indicates the overall scaling relation (used in Figure 14(a)), and the dashed blue and red lines indicate the fits to the star-forming and quiescent populations, respectively. Scatter about the velocity dispersion predicted by these relations is shown in the center (quiescent) and right (star-forming) panels. Scatter for all galaxies (in black), quiescent galaxies (red), and star-forming galaxies (blue) is indicated in the upper left corner of each panel. It is clear that although using the individual relations reduces the scatter in the mass Faber–Jackson relation very slightly ($\sim$0.01 dex), the 3D planes exhibit far lower scatter for star-forming and quiescent galaxies alike.

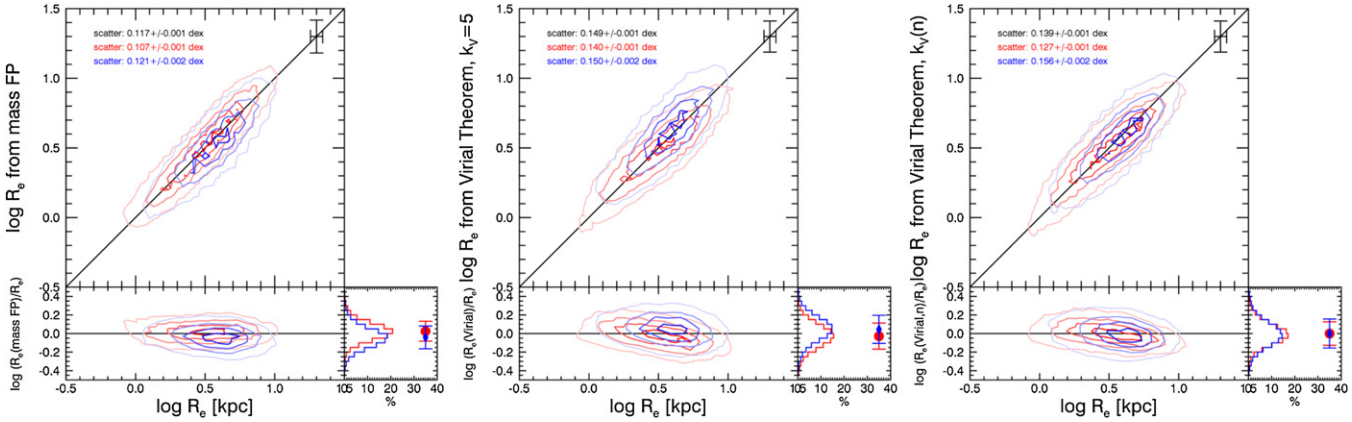

Figure 19. Scatter in log R_e in the SDSS from the mass fundamental plane (left) and the virial theorem with a fixed constant (center) and with a constant that depends on Sérsic index (right). The vertical axis in each is determined by the equations reported in Table 5.

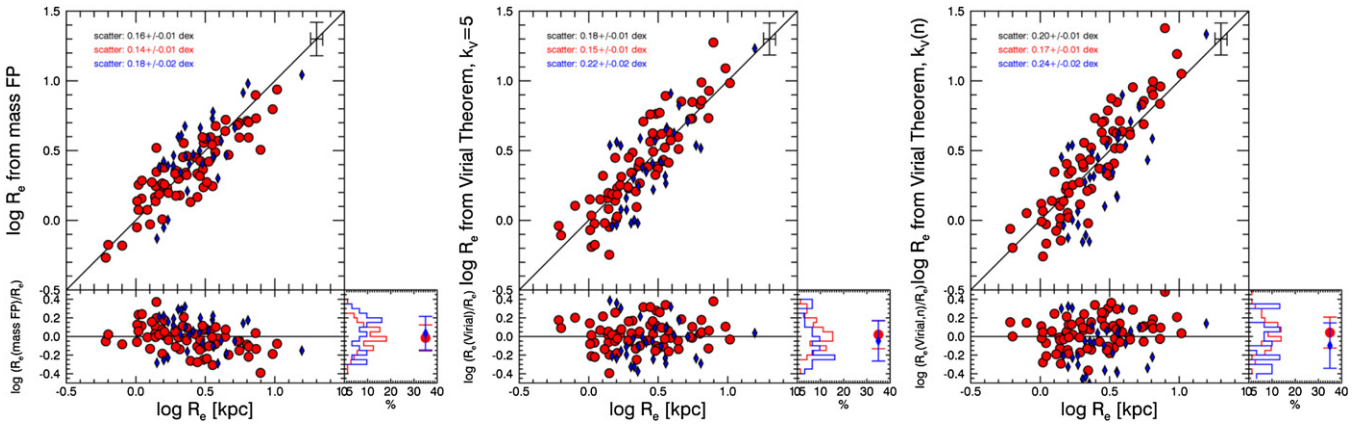

Figure 20. Scatter in log R_e at $z \sim 0.7$ from the mass fundamental plane (left panel) and the virial theorem with a fixed constant (center panel) and a Sérsic-dependent constant (right panel).

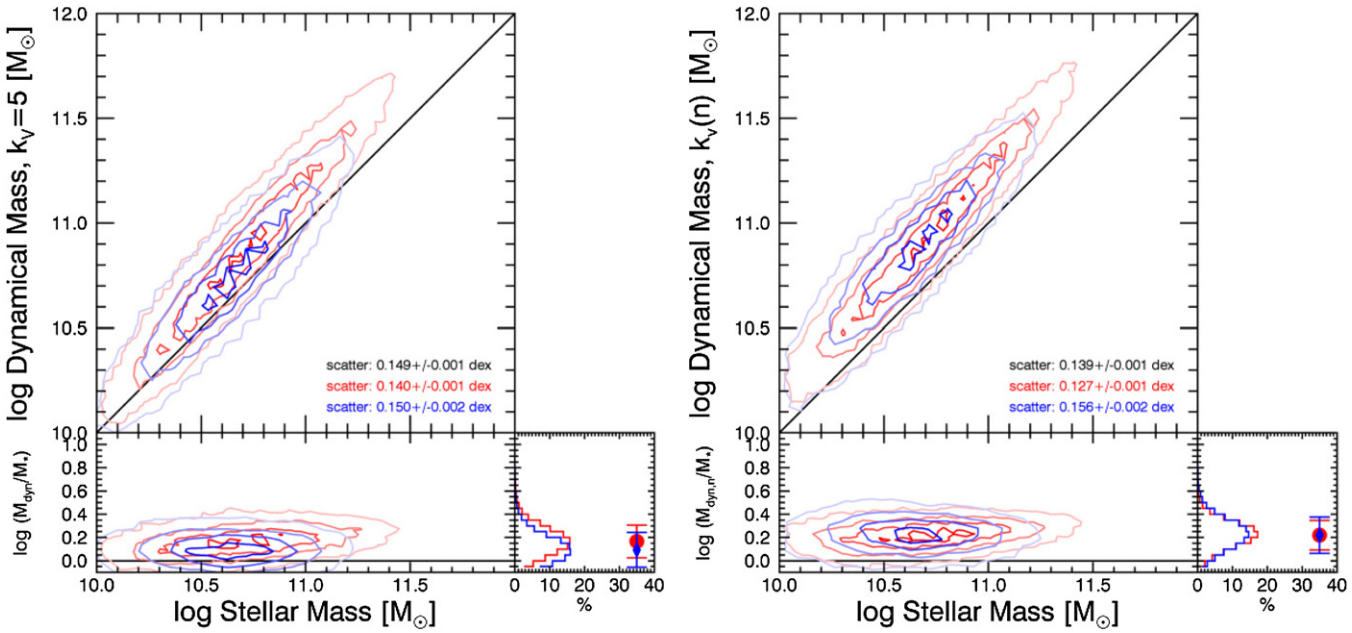

Figure 21. Dynamical and stellar masses of galaxies in the SDSS from the virial theorem with a fixed constant (left) and with a constant that depends on Sérsic index (right).

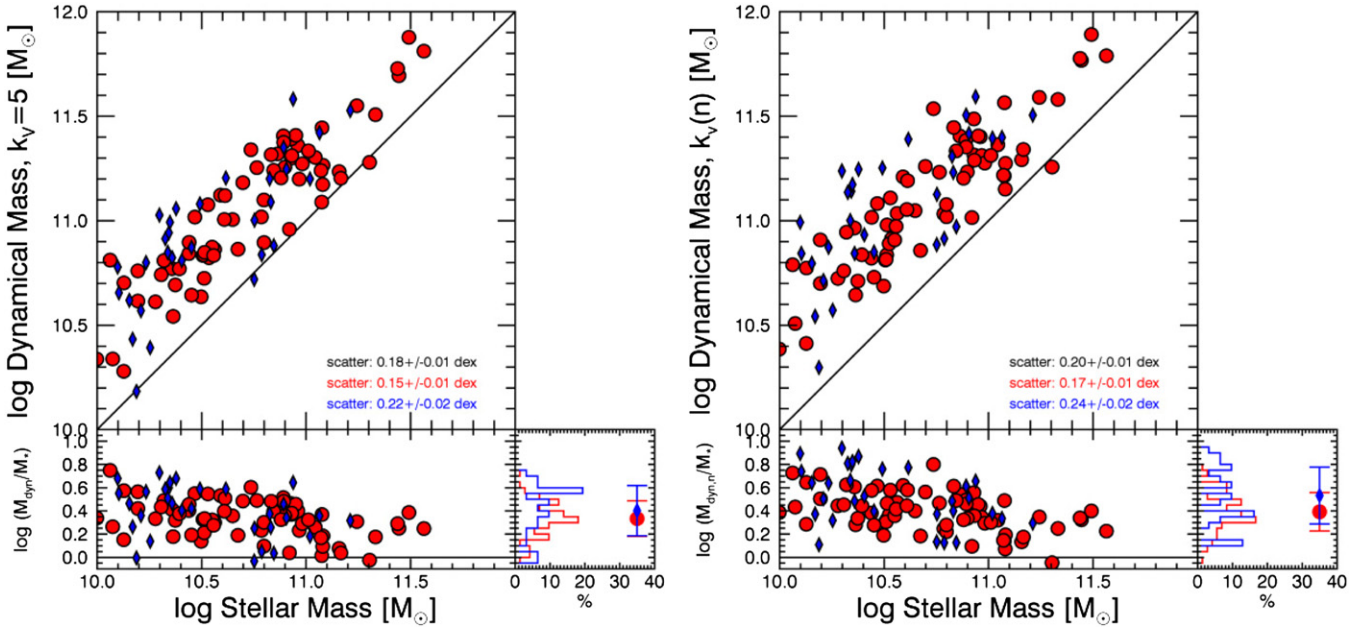

Figure 22. Dynamical and stellar masses of galaxies at $z \sim 0.7$ from the virial theorem with a fixed constant (left) and with a constant that depends on Sérsic index (right).

APPENDIX C

THREE-PARAMETER SCALING RELATIONS: SCATTER ABOUT log R_e

In this appendix we investigate the scatter in the mass fundamental plane and the virial relations in an additional projection (see also Figures 11(b), 12, and 13). For each relation, we calculate the scatter about log R_e. The slopes of the scaling relations are held fixed, but in each case the normalization is allowed to vary, although this will not affect the scatter. Best-fit normalizations, measured and intrinsic scatter, as determined through Monte Carlo simulations, are included in Table 5. Figure 19 illustrates the scatter about log R_e in the SDSS. The left panel includes sizes inferred by the mass fundamental plane, the center panel from the virial theorem with a fixed constant, and the right panel with a Sérsic-dependent constant. Figure 20 follows the same layout but includes galaxies in the DEIMOS sample. Unlike the scatter in velocity dispersion (see Figures 14 and 15), the scatter in the mass fundamental plane is significantly tighter than that of the virial relations. However, we expect this to be due, at least in part, to correlated errors in sizes and stellar mass surface densities. In this projection, the difference in scatter between star-forming and quiescent populations is also significant, 0.01–0.03 dex at $z \sim 0$ and up to ~0.07 dex at $z \sim 0.7$, particularly when using $k_V(n)$.

APPENDIX D

VIRIAL ESTIMATES OF DYNAMICAL MASS

Throughout this paper we mention virial estimates of galaxy dynamical masses. Although all such measurements are calculated based on the virial theorem, dynamical mass estimates are sensitive to the choice of virial constant (see Section 5). Cappellari et al. (2006) derived an analytic form for the virial constant based on spherical Jeans models of mass-follows-light Sérsic models (Equation (6)) but found that a single-valued constant $k = 5$ is sufficient to describe the dynamical and structural properties within an effective radius of the elliptical galaxies in the local ATLAS3D sample. Furthermore, Taylor et al. (2009) demonstrated the importance of accounting for structural differences, as quantified by the Sérsic index, when determining the dynamics of massive galaxies in the SDSS. The latter work found that the dynamical mass of a galaxy is well correlated with its stellar mass as long as one adopts a virial constant that depends on Sérsic index, despite the structural nonhomology of the SDSS galaxy sample. Figures 21 and 22 explicitly show the relationship between stellar mass and dynamical mass in the SDSS and at $z \sim 0.7$. The left panel of each figure shows the dynamical mass calculated with a single virial constant relative to stellar mass, and the right panel includes $k_{V(n)}$.

In the left panel of Figure 21 we reproduce a main result from Taylor et al. (2009): the scatter is decreased and overall correlation between dynamical and stellar masses for SDSS galaxies is improved when structural nonhomology is included in dynamical mass calculations (in the right panel relative to the left panel). This relation is less apparent for galaxies in the $z \sim 0.7$ sample (Figure 22). In this case, the scatter is similar within the errors for both relations, and if anything the scatter increases in the right panel (with $k_V(n)$). We note that this difference suggests that perhaps the analytic form that we adopt for the Sérsic dependence of the virial constant may no longer be optimal at high z. However, the modeling of these galaxies including differences in extraction apertures, seeing, velocity dispersion profiles used for aperture corrections, and possibly structural evolution is beyond the scope of this paper.

REFERENCES

Abazajian, K. N., Adelman-McCarthy, J. K., Agüeros, M. A., et al. 2009, ApJS, 182, 543
Barro, G., Faber, S. M., Pérez-González, P. G., et al. 2013, ApJ, 765, 104
Barro, G., Faber, S. M., Perez-Gonzalez, P. G., et al. 2014a, ApJ, 791, 52
Barro, G., Trump, J. R., Koo, D. C., et al. 2014b, ApJ, 795, 145
Bell, E. F., & de Jong, R. S. 2001, ApJ, 550, 212
Bell, E. F., Wolf, C., Meisenheimer, K., et al. 2004, ApJ, 608, 752
Belli, S., Newman, A. B., & Ellis, R. S. 2014a, ApJ, 783, 117
Belli, S., Newman, A. B., Ellis, R. S., & Konidaris, N. P. 2014b, ApJL, 788, L29

Bertin, G., Ciotti, L., & Del Principe, M. 2002, A&A, 386, 149
Bezanson, R., van Dokkum, P., & Franx, M. 2012, ApJ, 760, 62
Bezanson, R., van Dokkum, P. G., Franx, M., et al. 2011, ApJL, 737, L31
Bezanson, R., van Dokkum, P. G., Tal, T., et al. 2009, ApJ, 697, 1290
Bezanson, R., van Dokkum, P. G., van de Sande, J., et al. 2013, ApJL, 779, L21
Bielby, R., Hudelot, P., McCracken, H. J., et al. 2012, A&A, 545, A23
Blanton, M. R., Hogg, D. W., Bahcall, N. A., et al. 2003, ApJ, 594, 186
Blanton, M. R., & Roweis, S. 2007, AJ, 133, 734
Blanton, M. R., Schlegel, D. J., Strauss, M. A., et al. 2005, AJ, 129, 2562
Blumenthal, G. R., Faber, S. M., Flores, R., & Primack, J. R. 1986, ApJ, 301, 27
Brammer, G. B., van Dokkum, P. G., Franx, M., et al. 2012, ApJS, 200, 13
Brammer, G. B., Whitaker, K. E., van Dokkum, P. G., et al. 2011, ApJ, 739, 24
Brinchmann, J., Charlot, S., White, S. D. M., et al. 2004, MNRAS, 351, 1151
Bruce, V. A., Dunlop, J. S., Cirasuolo, M., et al. 2012, MNRAS, 427, 1666
Bruzual, G., & Charlot, S. 2003, MNRAS, 344, 1000
Cappellari, M., Bacon, R., Bureau, M., et al. 2006, MNRAS, 366, 1126
Cappellari, M., & Emsellem, E. 2004, PASP, 116, 138
Cappellari, M., McDermid, R. M., Alatalo, K., et al. 2013a, MNRAS, 432, 1862
Cappellari, M., Scott, N., Alatalo, K., et al. 2013b, MNRAS, 432, 1709
Chabrier, G. 2003, PASP, 115, 763
Chang, Y.-Y., van der Wel, A., Rix, H.-W., et al. 2013, ApJ, 773, 149
Chevance, M., Weijmans, A.-M., Damjanov, I., et al. 2012, ApJL, 754, L24
Ciotti, L. 1991, A&A, 249, 99
Cooper, M. C., Newman, J. A., Davis, M., Finkbeiner, D. P., & Gerke, B. F. 2012, spec2d: DEEP2 DEIMOS Spectral Pipeline (Astrophysics Source Code Library)
Daddi, E., Renzini, A., Pirzkal, N., et al. 2005, ApJ, 626, 680
Djorgovski, S., & Davis, M. 1987, ApJ, 313, 59
Dressler, A., Lynden-Bell, D., Burstein, D., et al. 1987, ApJ, 313, 42
Erben, T., Hildebrandt, H., Lerchster, M., et al. 2009, A&A, 493, 1197
Faber, S. M. (ed.) 1987, in Proceedings of the Eighth Santa Cruz Summer Workshop in Astronomy and Astrophysics, Santa Cruz, CA, Nearly Normal Galaxies: From the Planck Time to the Present (New York: Springer), 175
Faber, S. M., & Jackson, R. E. 1976, ApJ, 204, 668
Faber, S. M., Phillips, A. C., Kibrick, R. I., et al. 2003, Proc. SPIE, 4841, 1657
Fall, S. M., & Efstathiou, G. 1980, MNRAS, 193, 189
Franx, M., van Dokkum, P. G., Schreiber, N. M. F., et al. 2008, ApJ, 688, 770
Furusawa, H., Kosugi, G., Akiyama, M., et al. 2008, ApJS, 176, 1
Grogin, N. A., Kocevski, D. D., Faber, S. M., et al. 2011, ApJS, 197, 35
Guo, Y., McIntosh, D. H., Mo, H. J., et al. 2009, MNRAS, 398, 1129
Hildebrandt, H., Pielorz, J., Erben, T., et al. 2009, A&A, 498, 725
Hilz, M., Naab, T., & Ostriker, J. P. 2013, MNRAS, 429, 2924
Holden, B. P., van der Wel, A., Kelson, D. D., Franx, M., & Illingworth, G. D. 2010, ApJ, 724, 714
Holden, B. P., van der Wel, A., Rix, H.-W., & Franx, M. 2012, ApJ, 749, 96
Hopkins, P. F., Bundy, K., Murray, N., et al. 2009a, MNRAS, 398, 898
Hopkins, P. F., Hernquist, L., Cox, T. J., Keres, D., & Wuyts, S. 2009b, ApJ, 691, 1424
Hyde, J. B., & Bernardi, M. 2009, MNRAS, 396, 1171
Isobe, T., Feigelson, E. D., Akritas, M. G., & Babu, G. J. 1990, ApJ, 364, 104
Jørgensen, I., & Chiboucas, K. 2013, AJ, 145, 77
Jorgensen, I., Franx, M., & Kjaergaard, P. 1996, MNRAS, 280, 167
Kassin, S. A., Weiner, B. J., Faber, S. M., et al. 2007, ApJL, 660, L35
Koekemoer, A. M., Aussel, H., Calzetti, D., et al. 2007, ApJS, 172, 196
Koekemoer, A. M., Faber, S. M., Ferguson, H. C., et al. 2011, ApJS, 197, 36
Kriek, M., van Dokkum, P. G., Labbé, I., et al. 2009, ApJ, 700, 221
Martin, D. C., Fanson, J., Schiminovich, D., et al. 2005, ApJL, 619, L1
Massey, R., Stoughton, C., Leauthaud, A., et al. 2010, MNRAS, 401, 371
Miller, S. H., Ellis, R. S., Sullivan, M., et al. 2012, ApJ, 753, 74
Mo, H. J., Mao, S., & White, S. D. M. 1998, MNRAS, 295, 319
Muzzin, A., Marchesini, D., Stefanon, M., et al. 2013, ApJ, 777, 18
Muzzin, A., Marchesini, D., van Dokkum, P. G., et al. 2009, ApJ, 701, 1839
Nelson, E., van Dokkum, P., Franx, M., et al. 2014, Natur, 513, 394
Newman, J. A., Cooper, M. C., Davis, M., et al. 2013, ApJS, 208, 5
Onodera, M., Renzini, A., Carollo, M., et al. 2012, ApJ, 755, 26
Patel, S. G., van Dokkum, P. G., Franx, M., et al. 2013, ApJ, 766, 15
Peng, C. Y., Ho, L. C., Impey, C. D., & Rix, H.-W. 2002, AJ, 124, 266
Rousseeuw, P. J., & van Driessen, K. 2006, Data Mining and Knowledge Discovery, 12, 29
Shen, S., Mo, H. J., White, S. D. M., et al. 2003, MNRAS, 343, 978
Simard, L., Mendel, J. T., Patton, D. R., Ellison, S. L., & McConnachie, A. W. 2011, ApJS, 196, 11
Skelton, R. E., Whitaker, K. E., Momcheva, I. G., et al. 2014, ApJS, 214, 24
Straatman, C. M. S., Labbé, I., Spitler, L. R., et al. 2014, ApJL, 783, L14
Szomoru, D., Franx, M., van Dokkum, P. G., et al. 2010, ApJL, 714, L244
Tacconi, L. J., Genzel, R., Smail, I., et al. 2008, ApJ, 680, 246
Taniguchi, Y., Scoville, N., Murayama, T., et al. 2007, ApJS, 172, 9
Taylor, E. N., Franx, M., Brinchmann, J., van der Wel, A., & van Dokkum, P. G. 2010, ApJ, 722, 1
Taylor, E. N., Franx, M., van Dokkum, P. G., et al. 2009, ApJS, 183, 295
Toft, S., Gallazzi, A., Zirm, A., et al. 2012, ApJ, 754, 3
Toft, S., Smolcic, V., Magnelli, B., et al. 2014, ApJ, 782, 68
Tomczak, A. R., Quadri, R. F., Tran, K.-V. H., et al. 2014, ApJ, 783, 85
Trujillo, I., Förster Schreiber, N. M., Rudnick, G., et al. 2006, ApJ, 650, 18
Tully, R. B., & Fisher, J. R. 1977, A&A, 54, 661
van der Wel, A., Bell, E. F., Häussler, B., et al. 2012, ApJS, 203, 24
van der Wel, A., Franx, M., van Dokkum, P. G., & Rix, H.-W. 2004, ApJL, 601, L5
van der Wel, A., Franx, M., van Dokkum, P. G., et al. 2014, ApJ, 788, 28
van der Wel, A., Rix, H.-W., Wuyts, S., et al. 2011, ApJ, 730, 38
van de Sande, J., Kriek, M., Franx, M., et al. 2011, ApJL, 736, L9
van de Sande, J., Kriek, M., Franx, M., et al. 2013, ApJ, 771, 85
van Dokkum, P. G., & Franx, M. 1996, MNRAS, 281, 985
van Dokkum, P. G., Franx, M., Kriek, M., et al. 2008, ApJL, 677, L5
van Dokkum, P. G., Kriek, M., & Franx, M. 2009, Natur, 460, 717
van Dokkum, P. G., & van der Marel, R. P. 2007, ApJ, 655, 30
van Dokkum, P. G., Whitaker, K. E., Brammer, G., et al. 2010, ApJ, 709, 1018
Vogt, N. P., Forbes, D. A., Phillips, A. C., et al. 1996, ApJL, 465, L15
Warren, S. J., Hambly, N. C., Dye, S., et al. 2007, MNRAS, 375, 213
Weiner, B. J., Willmer, C. N. A., Faber, S. M., et al. 2006a, ApJ, 653, 1027
Weiner, B. J., Willmer, C. N. A., Faber, S. M., et al. 2006b, ApJ, 653, 1049
Weinzirl, T., Jogee, S., Conselice, C. J., et al. 2011, ApJ, 743, 87
Whitaker, K. E., Kriek, M., van Dokkum, P. G., et al. 2012, ApJ, 745, 179
Whitaker, K. E., Labbe, I., van Dokkum, P. G., et al. 2011, ApJ, 735, 86
Williams, R. J., Quadri, R. F., Franx, M., van Dokkum, P., & Labbé, I. 2009, ApJ, 691, 1879
Zaritsky, D., Gonzalez, A. H., & Zabludoff, A. I. 2006, ApJ, 638, 725
Zaritsky, D., Zabludoff, A. I., & Gonzalez, A. H. 2008, ApJ, 682, 68
Zaritsky, D., Zabludoff, A. I., & Gonzalez, A. H. 2011, ApJ, 727, 116